Submitted to *Sensors*. Pages 1 - 41.

OPEN ACCESS

Article

Vision-based Detection and Distance Estimation of Micro Unmanned Aerial Vehicles

Fatih Gökçe [1]*, Göktürk Üçoluk [1], Erol Şahin [1] and Sinan Kalkan [1]

[1] Department of Computer Engineering, Middle East Technical University, Üniversiteler Mahallesi, Dumlupınar Bulvarı No:1 06800 Çankaya Ankara, TURKEY

* Author to whom correspondence should be addressed; E-mail: fgokce@ceng.metu.edu.tr; Tel.: +90-312-210-5545; Fax.: +90-312-210-5544

Version August 19, 2015 submitted to Sensors. *Typeset by LATEX using class file mdpi.cls*

Abstract: Detecting Micro Unmanned Aerial Vehicles (mUAVs) is crucial for (i) multi-UAV control scenarios such as environmental monitoring, surveillance and exploration as well as (ii) for intrusion detection by mUAVs in protected environments. In this article, we focus on visual detection and localization of mUAVs for these purposes. We evaluate vision algorithms as alternatives for detecting and localizing mUAVs, since other sensing modalities entail certain limitations on the environment or the distance between the UAVs. For this purpose, we test Haar-like features, Histogram of Gradients (HOG) and Local Binary Patterns (LBP) using cascades of boosted classifiers. Cascaded boosted classifiers allow fast processing by performing detection tests at multiple stages, where only candidates passing earlier simple stages are processed at the preceding more complex stages. We also integrate a position estimation method to our system utilizing geometric cues with Support Vector Regressors. We evaluated each method with both indoor and outdoor test videos that are collected in a systematic way, and also with videos having motion blur. Our experiments show that, using boosted cascaded classifiers with LBP, near real-time detection and distance estimation of mUAVs are possible in about 60 ms indoors (1032×778 resolution) and 150 ms outdoors (1280×720 resolution) per frame, with a detection rate of 0.96 F-Score. However, the output of C-HAAR leads to better distance estimation since it can position the bounding boxes on mUAVs more accurately. On the other hand, our time analysis yields that C-HOG trains and runs faster than the other algorithms.

Keywords: UAV; micro UAV; vision; detection; localization, cascaded classifiers

1. Introduction

Advances in the development of micro Unmanned Aerial Vehicles (mUAVs)[1] has led to the availability of highly capable yet cheap flying platforms. This has made the deployment of mUAV systems in surveillance, monitoring and delivery tasks a feasible alternative. The use of mUAVs in monitoring the state of forest fires where the mission spreads over a large region, and flying over the fire is dangerous [2], or in delivering packages in urban areas [3] as a faster and cheaper solution is being explored. Moreover, the widespread interest in public has also resulted in mUAVs[2] showing up in places such as the White House where conventional security measures caught unprepared [4], or in traffic accidents of fires where the presence of mUAVs, flown by hobbyists to observe the scene, posed a danger to police and fire-fighter helicopters, and resulted in delays in their deployment [5]. In all these cases, the need for the automatic detection and localization of mUAVs, either from the ground or from a flying platform (which can be another mUAV or a helicopter) against a possibly cluttered background is apparent.

The main objective of our study is the evaluation of vision as a sensor for detecting and localizing mUAVs. This problem poses a number of challenges: First, mUAVs are small in size and often do not project a compact and easily segmentable image on the camera. Even in applications where the camera is facing upwards and can see the mUAV against rather smooth and featureless sky, the detection poses big challenges. In multi-mUAV applications where each platform is required to sense its neighbors, and in applications where the camera is placed on a pole or on a high building for surveillance, the camera is placed at a height same or higher than the incoming mUAV, and the image of the mUAV is likely to be blended against feature-rich trees and buildings, with possibly other moving objects in the background, the detection and localization problem becomes challenging. Moreover, in multi-mUAV applications, the vibration of the platform as well as the size, power, weight and computational constraints posed on the vision system also need to be considered.

Within this paper, we report our work towards the development of an mUAV detection and localization system. Specifically, we have created a system for automatic collection of data in a controlled indoor environment, proposed and implemented the cascaded approach with different features and evaluated the detection performance and computational load of these approaches with systematic experiments on indoor and outdoor datasets.

For cooperative operation of mUAVs and for also sense and avoid purposes, relative localization in 3D space which requires the estimation of both bearing and distance is critical. By detecting an mUAV in an image, relative bearing can be estimated easily. However, for distance estimation, additional computation is needed. Due to the scale estimation problem in monocular vision and excessive variability of possible appearances of an mUAV for the same distance, the problem is challenging. Considering the demand for the distance information, we also developed a method to estimate relative distance of a detected mUAV by utilizing the size of detection window. We have performed indoor experiments to evaluate the performance of this approach in terms of both distance and time-to-collision estimation.

---

[1] mUAVs are UAVs less than 5 kg [1].
[2] which are often referred to as *drones*

2. Related Studies

In this section, we discuss the relevant studies in three parts. In the first part, general computer vision approaches related with object detection and recognition are reviewed. The second and third parts summarize the efforts in the robotics literature to detect and localize mUAVs using computer vision and other modalities, respectively.

2.1. Object Detection and Recognition Approaches with Computer Vision

In Computer Vision and Pattern Recognition (CVPR), object detection and recognition has been extensively studied (see [6,7] for comprehensive reviews), with applications ranging from human detection, face recognition to car detection, scene classification [8–13]. The approaches to detection and recognition can be broadly categorized into two: keypoint-based approaches and cascaded-approaches.

2.1.1. Keypoint-based Approaches

In keypoint-based methods, CVPR usually detects salient points, called interest points or keypoints, in the "keypoint detection" phase. In this phase, regions in the image that are likely to have important information content are identified. The key points should be as distinctive as possible and should be invariant, i.e., detectable under various transformations. Popular examples of keypoint detectors include Fast Corner Detection (FAST) [14,15], Harris corner detection (HARRIS) [16], Maximally Stable Extremal Region extractor (MSER) [17], Good Features To Track (GFTT) [18] - see [19] for a survey of local keypoint detectors.

In the next phase of keypoint-based approaches, intensity information at these keypoints are used to represent the local information in the image invariant to transformations such as rotation, translation, scale and illumination. Examples of the keypoint descriptors include Speeded-up Robust Features (SURF) [20], Scale Invariant Feature Transform (SIFT) [21], Binary Robust Independent Elementary Features (BRIEF) [22], Oriented FAST and Rotated BRIEF (ORB) [23], Binary Robust Invariant Scalable Keypoints (BRISK) [24], Fast Retina Keypoint (FREAK) [25].

Extracted features are usually high dimensional (e.g., 128 in the case of SIFT, 64 in SURF, etc.), which makes it difficult to use distributions of features for object recognition or detection. To overcome this difficulty, the feature space is first clustered (e.g., using k-means), and the cluster labels are used instead of high-dimensional features for, e.g., deriving histograms of features for representing objects. This approach, called *bag-of-words* (BOW) model, has become very popular in object recognition (see, e.g., [26–28]). In BOW, histograms of cluster labels are used to train a classifier, such as Naive Bayes classifier or Support Vector Machines [29], to learn a model of the object.

In the testing phase of BOW, a window is slided over the image and for each position of the window in the image, a histogram of the cluster labels of the features in that window is computed and tested with the trained classifiers. However, the scale of the window imposes a severe limitation on the size of the object that can be detected or recognized. This limitation can be overcome to only a certain extent by sliding windows of different scales. However this introduces a significant computational burden, making it unsuitable for real-time applications.

2.1.2. Hierarchical and Cascaded Approaches

A better approach in CVPR is to employ hierarchical and cascaded models into recognition and detection. In such approaches, shape, texture and appearance information at different scales and complexities are processed, unlike the regular keypoint-based approaches. Processing at multiple levels has been shown to perform better than the alternative approaches (see, e.g., [30]).

In hierarchical approaches, such as the deep learning approaches [31], features of varying scale are processed at each level: in lower levels of the hierarchy, low-level visual information such as gradients, edges etc. are computed, and with increasing levels in the hierarchy, features of the lower-levels are combining, yielding corners or higher-order features that start to correspond to object parts and to objects. At the top of the hierarchy, object categories are represented hierarchically. For detecting an object in such an approach, the information needs to pass through all the hierarchies to be able to make a decision.

An alternative approach is to keep a multi-level approach but prune processing as early as possible if a detection does not seem likely. Such cascaded approaches, which are inspired, especially, from ensemble learning approaches [32] in machine learning, perform fast but coarse detection at early stages and only candidates passing earlier stages pass on to higher stages where finer details undergo computationally-expensive detailed processing. This way, these approaches benefit from speed by processing candidate regions that are highly likely to contain a match [33]. A prominent study, which also forms the basis of this study, is the approach by Viola and Jones [10,34], which builds cascades of Haar-based classifiers of varying complexities, adopting the Adaboost classifiers [35]. Viola and Jones [10,34] applied their method to face detection and demonstrated high detection rates at high speeds. The approach was later extended to work with Local Binary Patterns for face recognition [36] and Histogram of Oriented Gradients for human detection [37], which are more descriptive and faster to compute than Haar-like features.

2.2. Detection and Localization of mUAVs with Computer Vision

With advances in computational power, vision has become a feasible modality for several tasks with UAVs. These include fault detection [38], target detection [39] and tracking [40], surveillance [41,42], environmental sensing [43], state estimation and visual navigation [44–49], usually combined with other sensors such as GPS, Inertial Measurement Unit (IMU), altimeter or magnetometer.

Recently, vision has been used for mUAV detection and localization by recognizing black-and-white special markers placed on mUAVs [50,51]. In these studies, circular black-white patterns are designed and used for detection and distance estimation, achieving estimation errors less than 10 cm in real-time. However, in some applications where it is difficult to place markers on mUAVs, such approaches are not applicable and a generic vision-based detection system such as the one proposed in the current article is required.

In [52], leader-follower formation flight of two quadrotor mUAVs in outdoor environment is studied. Relative localization is obtained via monocular vision using boosted cascaded classifiers of HAAR-like features for detection and Kalman filtering for tracking. To estimate distance, they used the width of the leader with the camera model. They tested their vision based formation algorithm in simulation and with real mUAVs. Results for only real world experiments are provided where the follower tries to keep 6 m distance to the leader flying up to a speed of 2 m/s. Their results present only the relative distance of the mUAVs during a flight where the distance information is obtained probably (not mentioned clearly) from GPS. Although they claim that the tracking errors converge to zero, their results indicate that the errors always increase while the leader has a forward motion. Only when the leader becomes almost stationary after 35 seconds of total 105 seconds flight, the errors start to decrease.

In [53], 2D relative pose estimation problem is studied by extending the approach in [52]. Once mUAV is detected via cascaded classifier, its contours are extracted and for these contours best matching image from a set of images collected previously for different view angles is determined. Then, using affine transformation the orientation is estimated. Their experimental results are not sufficient to deduce the performance of pose estimation. Furthermore, they use the estimated pose to enhance relative distance estimation method applied in [52]. According to the results given for only 50 frames, there seems an improvement, however, the error is still very high (up to three meters for a 10 meters distance with a variance of 1.01 meters) and GPS is taken as the ground truth whose inherent accuracy is actually not very appropriate for such an evaluation.

Both studies [52,53] mentioned above use boosted cascaded classifiers for mUAV detection, however they provide no analysis about detection and computational performance of the classifiers. The methods are tested only outdoors and the results for the tracking and pose estimation are poor to evaluate the performances of the methods. They use HAAR-like features directly without any investigation. Moreover, no information is available about the camera and processing hardware used. The detection method is reported to run as 5 Hz.

In [54], collision detection problem for fixed-winged UAVs is studied. A morphological filter based on close-minus-open approach is used for preprocessing stage. Since morphological filters assume a contrast difference between the object and the background, once the image is preprocessed, the resulting candidate regions should be further inspected to get the final estimation. This is very crucial as the morphological filters produces large amount of false positives which have to be eliminated. For this purpose, they combined the morphological filtering stage with two different temporal filtering techniques, namely, Viterbi-based and Hidden Markov Model (HMM) based. The impact of image jitter and the performance of target detection are analyzed by off-board processing of video images on a graphical processing unit (GPU). For jitter analysis, videos recorded using a stationary camera are used by adding artificial jitter at three increasing levels, low, moderate and extreme. Both temporal filtering techniques demonstrate poor tracking performances in case of extreme jitter where interframe motion is greater than 4 pixels per frame. Some failure periods is also observed for HMM filter in moderate jitter case. Target detection performance experiments are performed on videos captured during three different flights with an onboard camera mounted on a UAV. Two of them include head on maneuvers and in the third one UAVs fly at right angles to each other. A detection range between 400 and 900 meters is reported allowing to estimate a collision before $8 - 10$ seconds of the impact.

There are also studies for detecting aircrafts via vision [55–57]. Although we include mainly the literature proposed for UAVs in this section, these studies are noteworthy since they are potentially useful for UAVs as long as size, weight and power (SWaP) constraints of UAVs are complied. In [55], aircraft detection under presence of heavily cluttered background patterns is studied for collision avoidance purposes. They applied a modified version of boosted cascaded classifiers using HAAR-like features for detection. Temporal filtering is also integrated to the system to reduce false positives by checking the previous detections around a detection before accepting it as valid. Their method does estimate the distance. Experimental results presented on videos recorded via a camera mounted on an aircraft and having collision course and crossing scenarios indicate a detection rate around 80% with up to 10 false positives per frame. No distance information is available between target and host aircrafts. Looking at the images, the distance seems to be on the order of some hundred meters. The performance of the system in close distances is also critical which is not clearly understood from their experiments. They report that their method has a potential of real time performance, however, no information is available about the frame size of the images and the processing hardware.

[56,57] present another approach for aircraft detection for sense and avoid purposes. They propose a detection method without distance estimation consisting of three stages which are (1) morphological filtering, (2) SVM-based classification of the areas found by stage 1, and (3) tracking based on similarity likelihoods of matching candidate detections. They tested their method on videos recorded using stationary cameras of various imaging sensor, lens and resolution options. These videos include aircraft flying only above horizon, therefore the background patterns are less challenging than below horizon case which is not investigated in the study. A detection rate of 98% at 5 statute miles with 1 false positive in every 50 frames is reported with a running time of 0.8 seconds for 4 megapixel frame.

Table 1. Comparison of the studies on visual detection of aerial vehicles.

Study	Vehicle	Detection Method	Detection Performance	Motion Blur	Training Time	Testing Time	Background Complexity	Environment	Distance Estimation
Lin et al., 2014	mUAV	Boosted cascaded classifiers with HAAR-like features	No	No	No	No	Medium	Outdoor	Yes (low accuracy)
Zhang et al., 2014	mUAV	Boosted cascaded classifiers with HAAR-like features	No	No	No	No	Medium	Outdoor	Yes (low accuracy)
Petridis et al., 2008	Aircraft	Boosted cascaded classifiers with HAAR-like features	Yes	No	No	No	High	Outdoor	No
Dey et al., 2009; 2011	Aircraft	Morphological filtering	Yes	No	NA	No	Low	Outdoor	No
Lai et al., 2011	mUAV	Morphological filtering	Yes	Yes	NA	Yes	High	Outdoor	No
Current study	mUAV	Boosted cascaded classifiers with HAAR-like, LBP and HOG features	Yes	Yes	Yes	Yes	High	Indoor and Outdoor	Yes

2.3. Detection and Localization of mUAVs with other Modalities

There are many alternative sensing methods that can be used for relative localization among mUAVs. One widely-used approach is Global Positioning System (GPS): In a cooperative scenario, each mUAV can be equipped with GPS receivers and share their positions with other agents [58]. However, GPS signals could be affected by weather, nearby hills, buildings, and trees. The service providers may also put limitations on the availability and accuracy of the GPS signals. Moreover, the accuracy of GPS signals is not sufficient for discriminating between close-by neighboring agents unless a Real-Time Kinematic GPS (RTK-GPS) system is used [59]. However, RTK-GPS systems require additional base station unit(s) located in the working environment.

Alternative to GPS, modalities such as (1) infrared [60–65], (2) audible sound signals [66,67], and (3) ultrasound signals [68–70] can be used; however, they entail certain limitations on the distance between the mUAVs and the environments in which they can perform detection. Infrared tends to be negatively affected from sunlight, hence not very suitable for outdoor applications. Sound can be a good alternative; yet, when there are close-by agents, interference becomes a hindrance for multi-mUAV systems and audible sound signals are prone to be affected from external sound sources. Multipath signals can disturb the measurements severely. The speed of the sound limits the achievable maximum update rate of the system. Moreover, current ultrasound transducers provide limited transmission and reception beam angles complicating the design of a system with omni-directional coverage.

An alternative modality commonly used by planes is radio waves (i.e., radar). The limitation with radar, however, is that the hardware is too heavy and expensive to place on an mUAV. Recently, there has been an effort to develop an X-Band radar to be used on mUAVs [71,72].

Ultra-wide band (UWB) radio modules which allow two-way time-of-flight and time-difference-of-arrival measurements, and signal strength between radio frequency (RF) devices could be thought as another alternatives. However, both techniques need anchor units placed at the environment. The use of UWB modules without beacon units could be considered as an aiding method to enhance the performance of localization systems that depend on other modalities. Signal strength between RF devices does not allow to design an accurate system due to uncertainties arising from antenna alignment and effects of the close objects.

2.4. The Current Study

As reviewed above, there is an interest in detecting and locating aerial vehicles via vision for various purposes such as cooperation and collision avoidance. Table 1 summarizes these studies in terms of various aspects. Looking at this comparison table and above explanations, our study fills a void with regard to the comprehensive and systematical analysis of cascaded methods with videos including very complex indoor and outdoor scenes providing also an accurate distance estimation method.

The main contribution of the article is a systematic analysis on whether a mUAV can be detected using a generic vision system under different motion patterns both indoors and outdoors. The tested indoor motion types include lateral, approach-leave, up-down and rotational motions that are precisely controlled using a physical platform that we constructed for the article. In the outdoor experiments, we tested both calm and agile motions that can also include moving background. Moreover, the effect of motion blur is also analyzed in a controlled manner. To the best of our knowledge, this is the first study that presents *comprehensive and systematical investigation* of the vision for detecting and localizing mUAVs without special requirements, e.g., markers used by [50,51].

Besides detecting the quadrotor, our study also integrates a distance estimation method in which a support vector regressor estimates the distance of the quadrotor utilizing the dimensions of the bounding box estimated in detection phase.

Since it is faster than the alternatives and it does not require a large training set, we use cascaded classifiers for detection, which consist of multiple (classification) stages with different complexities [10, 34,36,37]. The early (lower) stages of the classifier perform very basic checks to eliminate irrelevant windows with very low computational complexity. The windows passing the lower stages are low in

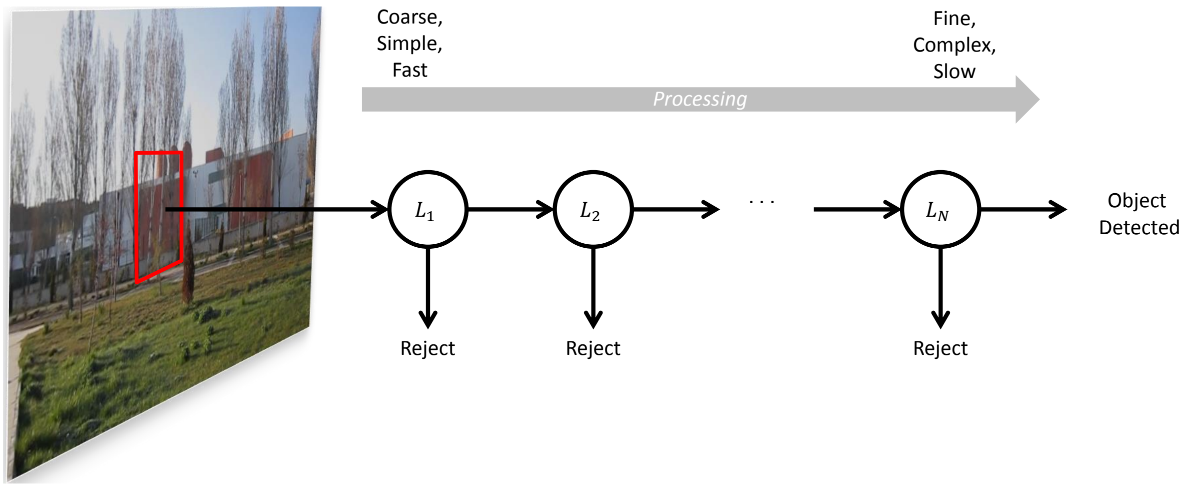

Figure 1. The stages of processing in a cascaded-approach. At each stage, a decision to reject or to continue processing is made. If all stages pass, then the method states detection of the object.

number, and undergo heavier computations to be classified as mUAV or background. To train a cascaded classifier, we use different feature types proposed in the literature and compare their performances.

3. Methods

In this section, we describe the cascaded detection methods used in this paper; namely, the method of Viola and Jones [10,34], and the ones that extend it [36,37].

3.1. A Cascaded Approach to mUAV Detection

Cascaded classifiers are composed of multiple stages with different processing complexities [10,34, 73]. Instead of one highly complex single processing stage, cascaded classifiers incorporate multiple stages with increasing complexities as shown in Figure 1.

Early stages of the classifier have lower computational complexities and are applied to the image to prune most of the search space quickly. The regions classified as mUAV by one stage of the classifier is passed to the higher stages. As the higher level of stages are applied, the classifier works on smaller number of regions at each stage to identify them as mUAV or background. At the end of last stage, the classifier returns the regions classified as mUAV.

In the method proposed by [10,34], which relies on using the AdaBoost learning, combinations of weak classifiers are used at each stage to capture an aspect of the problem to be learned. A weak classifier, $h_f(\mathbf{x})$, simply learns a linear classification for feature f with a threshold θ_f:

$$h_f(\mathbf{x}) = \begin{cases} 1 & \text{if } f(\mathbf{x}) < \theta_f \\ 0 & \text{otherwise} \end{cases} \tag{6}$$

The best performing weak classifiers are combined linearly to derive a stronger one (on a stage of the cascade) - see Algorithm 1.

In the approach of Viola & Jones [10,34], the AdaBoost algorithm is used to learn only one stage of the cascade of classifiers: In the cascade, simpler features are used in the earlier stages whereas bigger

Algorithm 1: AdaBoost Learning.

input : The training samples: $\{(\mathbf{x}_i, l_i)\}$, $i = 1, ..., N$, where $l_i = 1$ for positive, and $l_i = 0$ for negative samples. $N = m + o$, where m and o are the number of positives and negative samples, respectively.

output: Strong classifier, $h(\mathbf{x})$, as a combination of T weak classifiers.

- Initialize the weights for samples:
  $w_{1,i} = \frac{1}{2m}$ for positive samples, and $w_{1,i} = \frac{1}{2o}$ for negative samples.

for $t = 1$ *to* T **do**

- Normalize weights so that w_t add up to 1:

$$\hat{w}_{t,i} = \frac{w_{t,i}}{\sum_{j=1}^{n} w_{t,j}}. \tag{1}$$

for *each feature* $f \in \mathcal{F}$*, the set of all features* **do**

- Train a weak classifier h_f for learning from only feature f.
- Calculate the error of classification:

$$\epsilon_f = \sum_{i=1}^{n} \hat{w}_{t,i} |h_f(\mathbf{x}_i) - l_i|. \tag{2}$$

- Among the weak classifiers, h_f, $\forall f \in \mathcal{F}$, choose the one with the lowest error (ϵ_t):

$$h_t = \arg\min_{f \in \mathcal{F}} \epsilon_f. \tag{3}$$

- Update the weights:

$$w_{t+1,i} = \hat{w}_{t,i} \left(\frac{\epsilon_t}{1 - \epsilon_t} \right)^{e_i}, \tag{4}$$

where $e_i = 1$ if $\mathbf{x}_i$ is classified correctly, and 0 if it is not.

- The final classifier is then the combination of all the weak ones found above:

$$h(\mathbf{x}) = \begin{cases} 1 & \text{if} \sum_{t=1}^{T} \alpha_t h_t(\mathbf{x}) \geq \frac{1}{2} \sum_{t=1}^{T} \alpha_t \\ 0 & \text{otherwise} \end{cases} \tag{5}$$

where $\alpha_t = \log \frac{1-\epsilon_t}{\epsilon_t}$.

and more complex features are only processed if the candidate window passes the earlier stages. The method constructs the cascade by simply adding a new stage of AdaBoost classifier when the current cascade does not yield the desired false positive and detection rates - see Algorithm 2 and Figure 1.

Such an approach can only become computationally tractable if the features can be extracted in a very fast manner. One solution is using integral images, as proposed by Viola and Jones. In Section 3.1.1, we will describe them.

Algorithm 2: Learning a cascade of classifiers (Adapted from [34]).

input : Positive and negative training samples: $\mathcal{P} = \{\mathbf{x}_1^+, \mathbf{x}_2^+, ..., \mathbf{x}_L^+\}, \mathcal{N} = \{\mathbf{x}_1^-, \mathbf{x}_2^-, ..., \mathbf{x}_M^-\}$
output: The cascade of classifiers

initialize:
- $i = 0$: The stage number
- $F_i = 1.0$: False positive rate of the current cascaded classifier
- $D_i = 1.0$: Detection rate of the current cascaded classifier
- $\mathcal{N}_i = \mathcal{N}$: Negative samples for the current cascaded classifier
- f : user defined maximum acceptable false positive rate per layer
- d : user defined minimum acceptable detection rate per layer

while $F_i > F_{target}$ **do**
- $i \leftarrow i + 1$
- $n_i = 0$
- $F_i \leftarrow F_{i-1}$
- **while** $F_i > f \times F_{i-1}$ **do**
  - $n_i \leftarrow n_i + 1$
  - - Train a classifier h_{n_i} on $\mathcal{P}$ and N_i with n_i features using AdaBoost (see Algorithm 1)
  - - Determine F_i and D_i using the overall current cascaded detector
  - - Decrease threshold θ_i for h_{n_i} until $D_i > d \times D_{i-1}$
- **if** $F_i > F_{target}$ **then**
  - - Run the overall current cascaded detector with θ_i on $\mathcal{N}_0$
  - - Put any false negatives into $\mathcal{N}_{i+1}$

The cascaded detectors are usually run in multiple scales and locations, which lead to multiple detections for the same object. These are merged by looking at the amount of overlap between detections, as a post-processing stage.

3.1.1. Integral Images

In order to speed up the processing, computation of each feature in a window is performed using the integral images technique. In this method, for a pixel (i, j), the intensities of all pixels that have smaller row and column number are accumulated at (i, j):

$$II(i,j) = \sum_{c=1}^{i} \sum_{r=1}^{j} I(i,j), \tag{7}$$

where I is the original image, and II the integral image. Note that II can be calculated incrementally from the II of the neighboring pixels more efficiently.

Given such an integral image, the sum of intensities in a rectangular window can be calculated easily by accessing four values and performing 5 operations. See Figure 2 for an example: The sum of intensities in window A can be calculated as $II_4 + II_1 - (II_2 + II_3)$ [10].

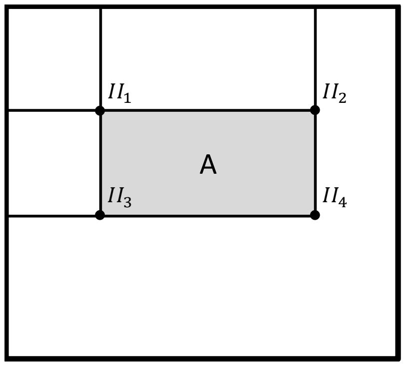

Figure 2. The method of integral images for efficient computation of sums of intensities in a window. The sum of intensities in window A can be calculated as $II_4 + II_1 - (II_2 + II_3)$. (Adapted from [10])

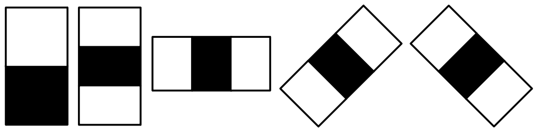

Figure 3. Sample Haar-like features used in our study.

3.2. Cascaded Detection using Haar Features (C-HAAR)

Haar-like features [74] are extensions of Haar wavelets to images. They can be used to extract meaningful information about the distribution of intensities in the form of various configurations of ON and OFF regions in an image window as shown in Figure 3. Combined with integral images, calculating the responses of Haar-like features at a pixel can be extremely sped-up, making it a suitable candidate for the cascaded approach.

In this paper, we are using the extended set of Haar-like features described in [73]. The detector window is run over the image at multiple scales and locations.

3.3. Cascaded Detection using Local Binary Patterns (C-LBP)

In LBP [75], a widely used method for feature extraction, a window is placed on each pixel in the image, and within which the intensity of the center pixel is compared against the intensities of the neighboring pixels. During this comparison, larger intensity values are taken as 1 and smaller values as 0. To describe formally, for a window $\Omega(x_c, y_c)$ at pixel (x_c, y_c) in image I, LBP pattern L_p is as $L_p(x_c, y_c) = \otimes_{(x,y)\in\Omega(x_c,y_c)}\sigma(I(x,y) - I(x_c, y_c))$, where $\otimes$ is the concatenation operator, and $\sigma(.)$ is the unit step function:

$$\sigma(x) = \begin{cases} 0 & \text{if } x < 0 \\ 1 & \text{otherwise} \end{cases} \tag{8}$$

The concatenation of 1's and 0's can be converted to a decimal number, representing the local intensity distribution around the center pixel with a single number:

$$L_2(x_c, y_c) = \sum_{i=0}^{|\Omega(x_c,y_c)|} 2^i \times L_p^i(x_c, y_c). \tag{9}$$

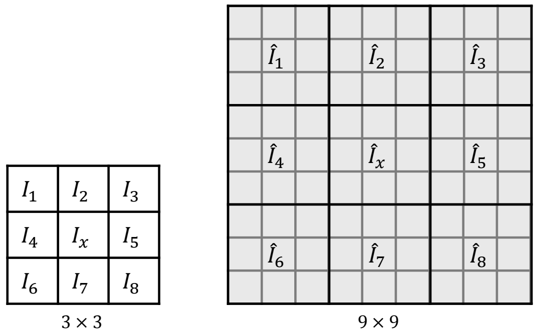

Figure 4. In LBP, the center pixel is compared with the others usually in a 3×3 window (left). In the multi-block version (on the right), average intensities in the blocks are compared instead.

The cascaded approach of Viola and Jones [10,34] has been extended by Liao et al. [36] to use a *statistically effective multi-scale* version of LBP (SEMB-LBP) features. In multi-scale LBP, instead of comparing the intensities of pixels, the average intensities of blocks in the window are compared with the central block - see Figure 4. Then, SEMB-LBP at scale s is defined as follows:

$$SEMB - LBP_s = \{\iota \mid rank(H_s(\iota)) < N\}, \tag{10}$$

where $rank(H_s)$ is the rank of H_s after descending sort; N is the number of uniform patterns, i.e., LBP binary strings where there are at most two 0-1 or 1-0 transitions in the string; and, H_s is the histogram at scale s:

$$H_s(\iota) = 1_{[f_s(x,y)=\iota]}, \qquad \iota = 0, ..., L-1, \tag{11}$$

where $f_s(x, y)$ is the outcome of the multi-scale LBP at pixel (x, y). In the current article, we test C-LBP with scales ($3 \times u, 3 \times v$) where $u = 1, ..., 13$ and $v = 1, ..., 7$, and N is set to 63, as suggested by [36]. To speed up the computation, integral images method is used on each bin of the histogram.

3.4. Cascaded Detection using Histogram of Oriented Gradients (C-HOG)

Histograms of Oriented Gradients (HOG) constructs a histogram of gradient occurrences in localized grid cells [11]. HOG has been demonstrated to be very successful in human detection and tracking. HOG of an image patch P is defined as follows:

$$HOG(k) = \sum_{p \in P} \delta\left(\left\lfloor \frac{\theta^p}{L} \right\rfloor \right), \tag{12}$$

where $\delta(\cdot)$ is the Kronecker delta given in Equation 8, L is a normalizing constant and θ^p is the orientation at point p, which is equal to the image gradient at that point. $HOG(k)$ corresponds to the value of the kth bin in a K-bin histogram. The value of K used in the experiments is set to 9, and the value of the normalizing constant, L, is equal to $180/K = 20$ [11].

Zhu et al. [37] extended HOG features so that the features are extracted at multiple-sizes of blocks at different locations and aspect ratios. This extension enables the definition of an increased number of blocks on which AdaBoost-based cascaded classification (Section 3.1) can be applied to choose the best combination. To speed up the computation, integral images method is used on each bin of the histogram.

3.5. Distance Estimation

Having detected the rectangle bounding an mUAV using one of the cascaded approaches introduced above, we can estimate its distance to the camera using the geometric cues. For this, we collect a training set of $\{(w_i, h_i), d_i\}$, where w_i, h_i are the width and the height of the mUAV bounding box, respectively, and d_i is the known distance of the mUAV. Having such a training set, we train a Support Vector Regressor (SVR - [76]). Using the trained SVR, we can estimate the distance of the mUAV once its bounding box is estimated.

4. Experimental Setup and Data Collection

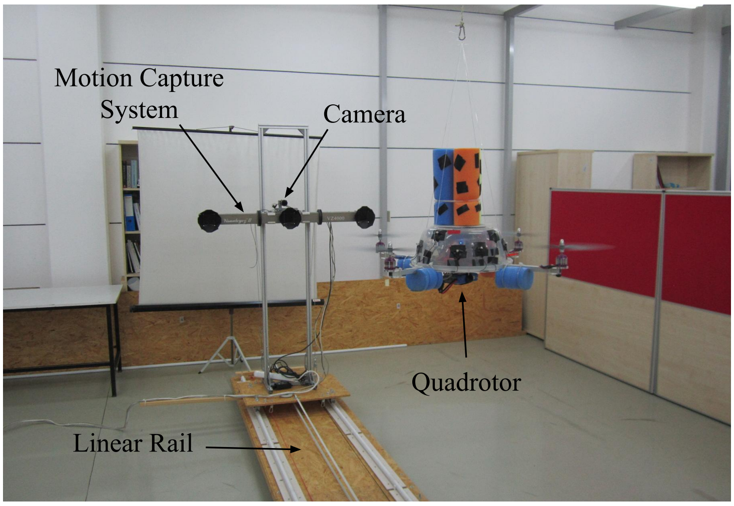

Figure 5. The setup used in indoor experiments. The rail was constructed in order to be able to move the camera with respect to the quadrotor in a controlled manner. This allows analyzing the performance of the methods under different motion types.

The experimental setup, shown in Figure 5, consists of the following components:

- **mUAV**: We used a quadrotor platform shown in Figure 6(a). Open-source Arducopter [77] hardware and software are used as the flight controller. The distance between the motors on the same axis is 60 cm. 12 markers are placed around the plastic cup of the quadrotor for which we define a rigid body. The body coordinate frame of the quadrotor is illustrated in Figure 6(a). x_Q-axis and y_Q-axis are towards the forward and right direction of the quadrotor, respectively. z_Q-axis points upwards with respect to the quadrotor.

- **Camera**: We use two different electro-optic cameras for indoor and outdoor due to varying needs in both environment. For indoor, the synchronization property of the camera is vital since we have to ensure that the 3D position data obtained from the motion capture system and the captured frames are synchronized in time. Complying this requirement, we use a camera from Basler Scout$^{\text{TM}}$ (capturing 1032×778 resolution videos at 30 fps in gray scale) mounted on top of the motion capture system. It weighs about 220 g including its lens whose maximum horizontal and vertical angle of views are $93.6°$ and $68.9°$, respectively. Power consumption of the camera is about 3 W and it outputs the data through Gigabit Ethernet port. The body coordinate frame of the camera is centered at the projection center. x_C-axis is towards the right side of the camera, y_C-axis points down of the camera, and z_C-axis coincides with the optical axis of the camera lens as depicted in Figure 6(b).

Due to difficulties in powering and recording of the indoor camera outdoors, we use another camera (Canon® PowerShot A2200 HD) to capture outdoor videos. This camera is able to record videos at 1280×720 resolution at 30 fps in color. However, we use gray scale versions of the videos in our study.

Although we needed to utilize a different camera outdoors due to logistic issues, we should note that our indoor camera is suitable to be placed on mUAVs in terms of SWaP constraints. Moreover, alternative cameras with similar image qualities compared to our cameras are also available in the market even with less SWaP requirements.

- **Motion capture system (used for indoor analysis)**: We use the Visualeyez™ II VZ4000 3D real-time motion capture system (MOCAP) (PhoeniX Technologies Incorporated) that can sense the 3D positions of active markers up to a rate of 4348 real-time 3D data points per second with an accuracy of $0.5 \sim 0.7$ mm RMS in ~ 190 cubic meters of space. In our setup, the MOCAP provides the ground truth 3D positions of the markers mounted on the quadrotor. The system provides the 3D data as labeled with the unique IDs of the markers. It has an operating angle of $90^\circ(\pm 45^\circ)$ in both pitch and yaw, and its maximum sensing distance is 7 m at minimum exposure. The body coordinate frame of the MOCAP is illustrated in Figure 6(c).
- **Linear rail platform (used for indoor analysis)**: We constructed a linear motorized rail platform to move the camera and the MOCAP together in a controlled manner so that we are able to capture videos of the quadrotor only with single motion types, i.e., approach-leave, up-down, lateral, rotational motions. With this platform, we are able to move the camera and MOCAP assembly on a horizontal line of approximately 5 meters up to 1 m/s speeds.

4.1. Ground Truth Extraction

In the indoor experimental setup, the MOCAP captures the motion of active markers mounted on the quadrotor, and supplies the ground truth 3D positions of those markers. For our purposes, we need the ground truth bounding box of the quadrotor and the distance between the quadrotor and the camera for each frame.

To determine a rectangular ground truth bounding box encapsulating the quadrotor in an image, we need to find a set of 2D pixel points (P'_{Qi})[3] on the boundaries of the quadrotor in the image. These 2D points correspond to a set of 3D points (P_{Qi}) on the quadrotor. To find P'_{Qi}, P_{Qi} should first be transformed from the body coordinate frame of the quadrotor to the MOCAP coordinate frame, followed

[3] In our derivations, all points in 2D or 3D sets are represented by homogeneous coordinate vectors.

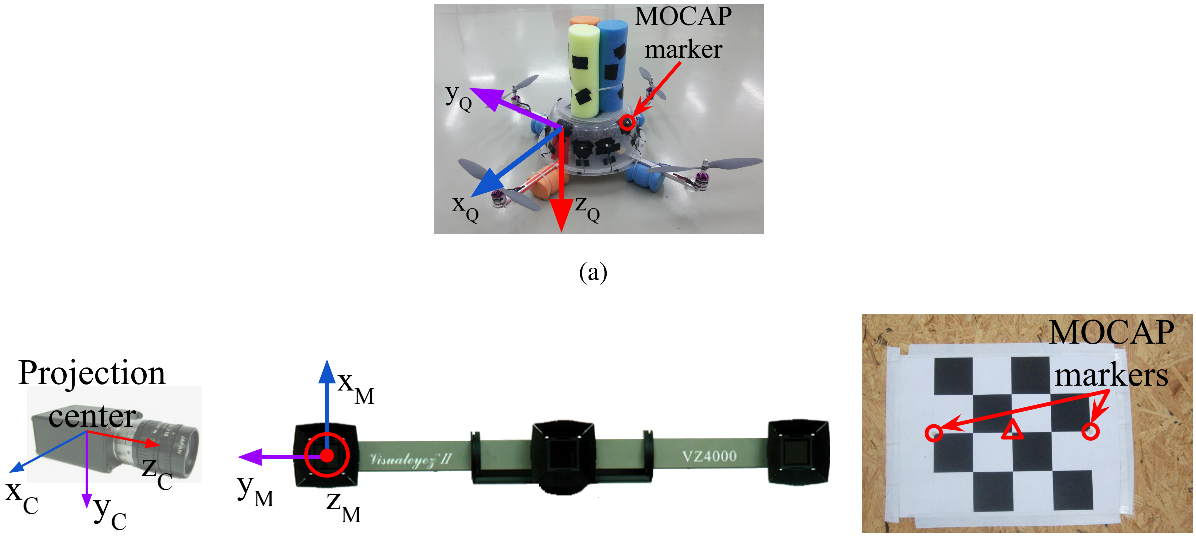

(b) (c) (d)

Figure 6. (a) The quadrotor used in our study and its body coordinate frame. There are 12 markers mounted roughly 30° apart from each other on the plastic cup of the quadrotor. (b) The Visualeyez$^{\text{TM}}$ II VZ4000 motion capture system and its body coordinate frame. (c) The body coordinate frame of the camera is defined at the projection center. (d) The calibration tool used to obtain 3D-2D correspondence points needed to estimate the transformation matrix, T_M^C, between the MOCAP and the camera coordinate systems. Circles and the triangle indicate the MOCAP markers and the center of the chess pattern, respectively.

by a transformation to the camera coordinate frame. These two transformations are represented by the transformation matrices T_Q^M and T_M^C, respectively, and are applied as follows:

$$P_{Mi} = T_Q^M P_{Qi} \text{ for all } i, \tag{13}$$

$$P_{Ci} = T_M^C P_{Mi} \text{ for all } i, \tag{14}$$

where P_{Mi} and P_{Ci} are the transformed coordinates in the MOCAP and the camera coordinate frames, respectively. After these transformations, we project the points in P_{Ci} to the image plane as:

$$P'_{Qi} = P_c P_{Ci} \text{ for all } i, \tag{15}$$

where P_c is the camera matrix and get P'_{Qi}. Then, we can find the bounding box of the quadrotor by calculating the rectangle with minimum size covering all of the points in P'_{Qi} as follows:

$$x_r = \min(x_i), \tag{16}$$

$$y_r = \min(y_i), \tag{17}$$

$$w_r = \max(x_i) - \min(x_i), \tag{18}$$

$$h_r = \max(y_i) - \min(y_i), \tag{19}$$

where $(x_i, y_i) \in P'_{Qi}$, (x_r, y_r) is the upper left pixel position of the rectangle, and w_r and h_r are the width and height of the rectangle, respectively.

It is not possible to place a marker on the quadrotor for every point in P_{Qi}. Therefore, we define a rigid body, a set of 3D points whose relative positions are fixed and remain unchanged under motion, for 12 markers on the quadrotor. The points in P_{Qi} are then defined virtually as additional points to the rigid body.

A rigid body can be defined from the positions of all markers obtained at a particular time instant while the quadrotor is stationary. However, we wanted to obtain a more accurate rigid body and used the method presented in [78,79] with multiple captures of the marker positions. Taking 60 different samples, we performed the following optimization to minimize the spatial distances between the measured points M_i and the points R_i in the rigid body model.

$$\arg\min_{R_i} \sum_i \|M_i - R_i\|^2, \tag{20}$$

where $\|.\|$ denotes the calculation of the Euclidean norm for the given vector.

Once the rigid body is defined for the markers on the quadrotor, if at least 4 markers are sensed by the MOCAP, T_Q^M can be estimated. Since the MOCAP supplies the 3D position data as labeled and the rigid body is already defined using these labels, there is no correspondence matching problem. Finding such a rigid transformation between two labeled 3D point sets requires the least square fitting of these two sets and is known as the "*Absolute Orientation Problem*" [80]. To solve this problem, we use the method presented in [78,81] and calculate T_Q^M. Note that T_Q^M transformation matrix should be calculated whenever the quadrotor or the camera moves with respect to each other.

There is no direct way of calculating T_M^C since it is not trivial to measure the distances and the angles between the body coordinate frames of the MOCAP and the camera. However, if we know a set of 3D points (P_{Ti}) in the MOCAP coordinate frame and a set of 2D points (P'_{Ti}) which corresponds to the projected pixel coordinates of the points in P_{Ti}, then we can estimate T_M^C as the transformation matrix that minimizes the re-projection error. The re-projection error is given by the sum of squared distances between the pixel points in P'_{Ti} as in the following optimization criterion:

$$\arg\min_{T_M^C} \sum_i \|P'_{Ti} - T_M^C P_{Ti}\|^2. \tag{21}$$

For collecting the data points in P_{Ti} and P'_{Ti}, we prepared a simple tool shown in Figure 6(d). In this tool, there is a chess pattern and 2 MOCAP markers mounted on the two edges of the chess pattern. 3D position of the chess pattern center, shown inside the triangle in Figure 6(d), is calculated by finding the geometric center of the marker positions. We obtain 2D pixel position of the chess pattern center using the camera calibration tools of Open Source Computer Vision Library (OpenCV) [82]. We collect the data need for P_{Ti} and P'_{Ti} by moving the tool in front the camera. Note that, since the MOCAP and the camera are attached to each other rigidly, once T_M^C is estimated, it is valid as long as the MOCAP and the camera assembly remained fixed.

To calculate the ground truth distance between the quadrotor and the camera, we use T_Q^M and T_M^C as follows:

$$p'_c = T_M^C T_Q^M p_c, \tag{22}$$

where p_c is 3D position of the quadrotor center in the quadrotor coordinate frame and $p_c^{'}$ is the transformed coordinates of the quadrotor center to the camera coordinate frame. p_c is defined as the geometric center of 4 points where the motor shafts and the corresponding propellers intersect. Once $p_c^{'}$ is calculated, the distance of the quadrotor to the camera (d_Q) is calculated as:

$$d_Q = \|p_c^{'}\|. \tag{23}$$

4.2. Data Collection for Training

Indoors: We recorded videos of the quadrotor by moving the MOCAP and the camera assembly around the quadrotor manually while the quadrotor is hanged at different heights from the ground and stationary with its motors running. From these videos, we automatically extracted 8876 image patches including only the quadrotor using the bounding box extraction method described in Section 4.1 without considering the aspect ratios of the patches. The distribution of the aspect ratios for these images are given in Figure 7 with a median value of 1.8168. Since the training of cascaded classifiers requires image windows with a fixed aspect ratio, we enlarged the bounding boxes of these 8876 images by increasing their width or height only according to the aspect ratio of the originally extracted image window, so that they all have a fixed aspect ratio of approximately 1.8168[4]. We preferred enlargement to fix the aspect ratios since this approach keeps all relevant data of the quadrotor inside the bounding box. We also recorded videos of the indoor laboratory environment without the quadrotor in the scene. From these videos, we extracted 5731 frames at a resolution of 1032×778 pixels as our background training image set. See Figures 8(a) and 8(b) for sample quadrotor and background images captured indoors.

Outdoors: We used a fixated camera to record while flying the quadrotor in front of the camera using remote control. Since the MOCAP is not operable outdoors, the ground truth is collected in a labor-extensive manner: By utilizing the background subtraction method presented in [83], we are able to approximate the bounding box of the quadrotor in these videos as long as there is not any moving object other than the quadrotor. Nevertheless, it is not always possible to get a motionless background. Therefore, the bounding boxes from background subtraction are inspected manually, and only the ones that bound the quadrotor well are selected. Both the number and aspect ratio of the outdoor training images are the same as the indoor images. For outdoor background training images, we have recorded videos at various places on the university campus. These videos include trees, bushes, grasses, sky, roads, buildings, cars and pedestrians without the quadrotor. From these videos, we have extracted frames as the same number of indoor background training images at 1280×720 resolution. See Figures 9(a) and 9(b) for sample images collected outdoors.

Looking at the training image sets, the following observations can be deduced which also represents the challenges in our problem: (i) Changes in camera pose or quadrotor pose result in very large differences of in quadrotor's visual appearance. (ii) The bounding box encapsulating the quadrotor contains large amount of background patterns due to structure of the quadrotor. (iii) Vibrations in the camera pose and agile motions of the quadrotor cause motion blur in the images. (iv) Changes

[4] Due to floating point rounding, aspect ratios may not be exactly 1.8168.

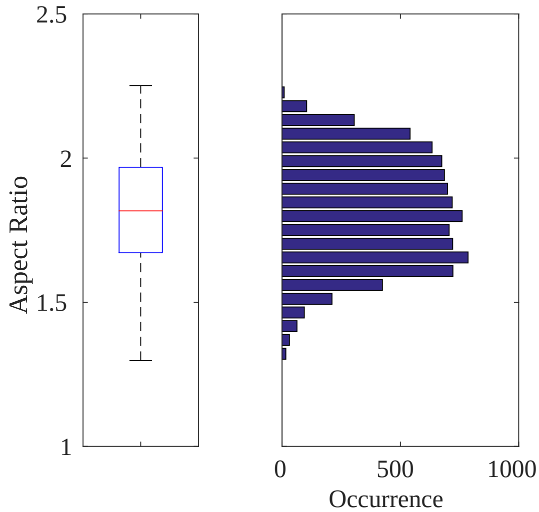

Figure 7. Box-plot (left) and histogram (right) representation for the aspect ratios of 8876 quadrotor images automatically extracted from the training videos. In this figure and the subsequent box-plot figures, the top and bottom edges of the box and the line inside the box represent the first and third quartiles and the median value, respectively. The bottom and top whiskers correspond to the smallest and largest non-outlier data, respectively. The data inside the box lie within the 50% confidence interval, while the data in between the whiskers lie within the 99.3% confidence interval. Here, the median value is 1.8168 which defines the aspect ratio of the training images used.

Figure 8. Example images from indoor (a) quadrotor and (b) background training image sets. Mostly the challenging examples are provided in the quadrotor images.

(a) (b)

Figure 9. Example images from outdoor (a) quadrotor and (b) background training image sets. The images are colored, however their grayscale versions are used in the training. For quadrotor images, mostly the challenging examples are included.

in brightness and the illumination direction yield very different images. (v) Motion in the image can also be induced by the motion of the camera or the motion of background objects (e.g., trees swinging due to wind, etc.).

4.3. Data Collection for Testing

Indoor and outdoor environments are significantly different from each other, since controlled experiments can only be performed indoors by means of motion capture systems. On the other hand, outdoor environments provide more space increasing the maneuverability of the quadrotor and many challenges that need to be evaluated. These differences directed us to prepare test videos of different characteristics indoors and outdoors.

In order to investigate the performance of the methods (C-HAAR, C-LBP and C-HOG) systematically, we defined 4 different motion types, namely, lateral, up-down, yaw and approach-leave for the indoor test videos. Please note that maneuvers in a free flight are combinations of these motions and use of these primitive motions is for systematical evaluation purposes. The recording procedure of each motion type is depicted in Figure 10 by two different views, the top view and the camera view. Each motion type has different characteristics in terms of the amount of changes in the scale and appearance of the quadrotor, and the background objects as shown in Table 2. Details of each motion type are as follows:

Table 2. Properties of motion types in terms of the amount of changes in the *scale* and *appearance* of the quadrotor, and the *background* objects.

	Lateral	Up-Down	Yaw	Approach-Leave
Scale	Moderate	Moderate	Small	Large
Appearance	Moderate	Large	Large	Large
Background	Large	No Change	No Change	Moderate

- **Lateral:** The camera performs left-to-right or right-to-left maneuvers while the quadrotor is fixed at different positions as illustrated in Figure 10. As seen in the top view, the perpendicular distance of the quadrotor to the camera motion course is changed by 1 m for each of 5 distances. For each

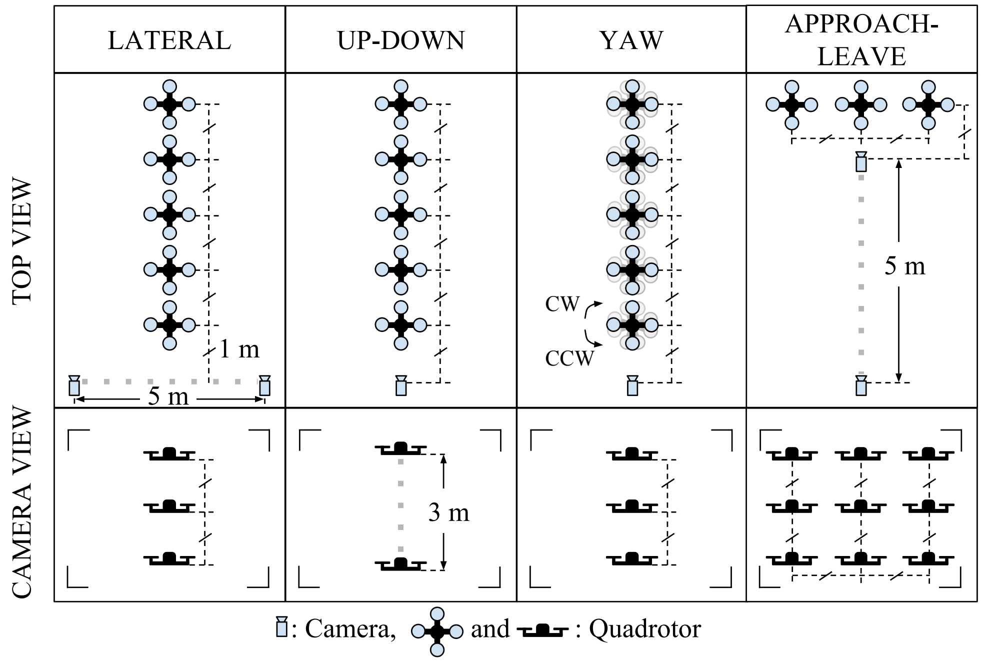

Figure 10. Graphical representation for indoor test videos. There are 4 motion types, namely, lateral, up-down, yaw and approach-leave. Each of them is illustrated with the top and camera views. Dashed gray thick lines represent the motion of the camera or the quadrotor along the path with given length. Dashed black thin lines are used to represent dimensions.

distance, the height of the quadrotor is adjusted to 3 different (top, middle and bottom) levels with 1 m apart making a total of 15 different position for lateral videos. Left-to-right and right-to-left videos collected in this manner allow us to test the features' resilience against large background changes.

In each video, the camera is moved along an approximately 5 m path. However, when the perpendicular distance is 1 m and 2 m and, the quadrotor is not fully visible in the videos for the top and bottom levels. Therefore, these videos are excluded from the dataset resulting in 22 videos with a total of 2543 frames.

- **Up-Down:** The quadrotor performs a vertical motion from the floor to the ceiling for the up motion and vice versa for the down motion. The motion of the quadrotor is performed manually with the help of a hanging rope. The change in the height of the quadrotor is approximately 3 m in each video. During the motion of the quadrotor, the camera remains fixed. For each of the 5 different positions shown in Figure 10, one up and one down video are recorded, resulting in 10 videos with a total of 1710 frames. These videos are used for testing the features' resilience against large appearance changes.
- **Yaw:** Quadrotor turns around itself in clockwise or counter clockwise directions while both the camera and the quadrotor are stationary. The quadrotor is positioned at the same 15 different points used in the lateral videos. Since the quadrotor is not fully present in the videos recorded for the top and bottom levels when the perpendicular distance is 1 m and 2 m, these videos are omitted from

the dataset. Hence, there are 22 videos with a total of 8107 frames in this group. These videos are used for testing the features' resilience against viewpoint changes causing large appearance changes.

- **Approach-Leave:** In these videos, the camera approaches the quadrotor or leaves away from it while the quadrotor is stationary. There are 9 different positions for the quadrotor with 1 m distance separation as illustrated in Figure 10. The motion path of the camera is approximately 5 m. By recording approach and leave videos separately, we have 18 videos with a total of 3574 frames for this group. These videos are used for testing whether the features are affected by large scale and appearance changes.

We should note that the yaw orientation of the quadrotor is set to random values for each of 50 videos in lateral, up-down and approach-leave sets, although the quadrotors in Figure 10 are given for a fixed orientation. There are cases where the MOCAP can give wrong or insufficient data to extract ground truth for some frames. These frames are not included in the dataset.

For outdoor experiments, we prepared four different videos with distinct characteristics. In all videos, the quadrotor is flown manually in front of a stationary camera. In the first two videos, a stationary background is chosen. These two videos differ in terms of agility such that in the first video the quadrotor performs *calm* maneuvers whereas in the second one it is flown *agile*. In the third video, the background includes moving objects like cars, motorcycles, bicycles and pedestrians while the quadrotor is flown in a calm manner. Fourth video is recorded to test maximum detection distances of the methods. In this video, the quadrotor first leaves away from the camera and then comes back flying on an approximately straight 110 meters path. We will call these videos as (i) Calm, (ii) Agile, (iii) Moving background, and (iv) Distance in the rest of the paper. These videos have 2954, 3823, 3900, and 2468 frames respectively. The ground truth bounding boxes for each frame of these three videos are extracted manually. For distance video, only ground truth distance of the quadrotor to the camera is calculated by utilizing another video recoded simultaneously by a side view camera. With the help of poles at known locations on the experiment area and by manually extracting the center of the quadrotor on the side view video, we computed the ground truth distance with simple geometrical calculations.

We should note that the scenes used in testing videos are different from the ones included in the training datasets for both indoor and outdoor.

5. Results

We implemented the cascaded methods introduced in Section 3 using OpenCV [82] and evaluated them on the indoor and outdoor datasets. We trained indoor and outdoor cascade classifiers separately using the corresponding training datasets with the following parameters: The quadrotor image windows were resized to 40×22 pixels. For an image with this window size, C-HAAR extracts 587408 features, whereas C-LBP and C-HOG yield 20020 and 20 features, respectively. 7900 positive (quadrotor) and 10000 negative (background) samples were used for indoors and outdoors. We trained the classifiers with 11, 13, 15, 17 and 19 stages (the upper limit of 19 is due to the enormous time required to train C-HAAR classifiers as will be presented in Section 5.6.1). During our tests the classifiers performed multi-scale detections beginning from a minimum window size of 80×44 and enlarging the window size by multiplying it with 1.1 at each scale.

5.1. Performance Metrics

To evaluate the detection performance of the classifiers, we use precision-recall (PR) curves, which are drawn by changing the threshold of the classifiers' last stages from -100 to $+100$, as performed by [10,34]. Note that each stage of the cascaded classifiers has its own threshold determined during the training, and that increasing the threshold of a stage S to a high value such as $+100$ results in a classifier with $S-1$ many stages at the default threshold.

Precision is defined as:

$$Precision = \frac{tp}{tp + fp}, \tag{24}$$

where tp is the number of true positives (see below), and fp is the number of false positives. Recall is defined as:

$$Recall = \frac{tp}{tp + fn}, \tag{25}$$

where fn is the number of false negatives.

A detected bounding box (B_D) is regarded as a true positive if its Jaccard Index (J) [84], calculated as follows, is greater than 60%:

$$J(B_D, B_G) = \frac{|B_D \cap B_G|}{|B_D \cup B_G|}, \tag{26}$$

where B_G is the ground truth bounding box. Otherwise, B_D is regarded as a false positive. If there are multiple detections in a frame, each B_D is evaluated separately as a tp or fp. If no B_D is found for an image frame by the classifier, then fn is incremented by one.

We use also F-Score in our evaluations calculated as follows:

$$F\text{-}Score = 2 \times \frac{Precision \times Recall}{Precision + Recall}. \tag{27}$$

A widely-used measure with PR-curves is the normalized area under curve. If a PR curve, $p(x)$, is defined at the interval $[r_{min}, r_{max}]$, where r_{min} and r_{max} are the minimum and maximum recall values, respectively, the normalized area A_p under curve $p(x)$ is defined as:

$$A_p = \frac{1}{r_{max} - r_{min}} \int_{r_{min}}^{r_{max}} p(x)\, dx. \tag{28}$$

5.2. Indoor Evaluation

We tested the classifiers trained with indoor training dataset, on indoor test videos having 15934 frames in total with four different motion types, namely, lateral, up-down, yaw and approach-leave as presented in Section 4.3. We evaluated the classifiers for 5 different number of stages to understand how they perform while their complexity increases. Figure 11 shows the PR curves as well as the normalized area under the PR curves for each method and for different number of stages. In Table 3, the maximum F-Score values and the values at default thresholds are listed.

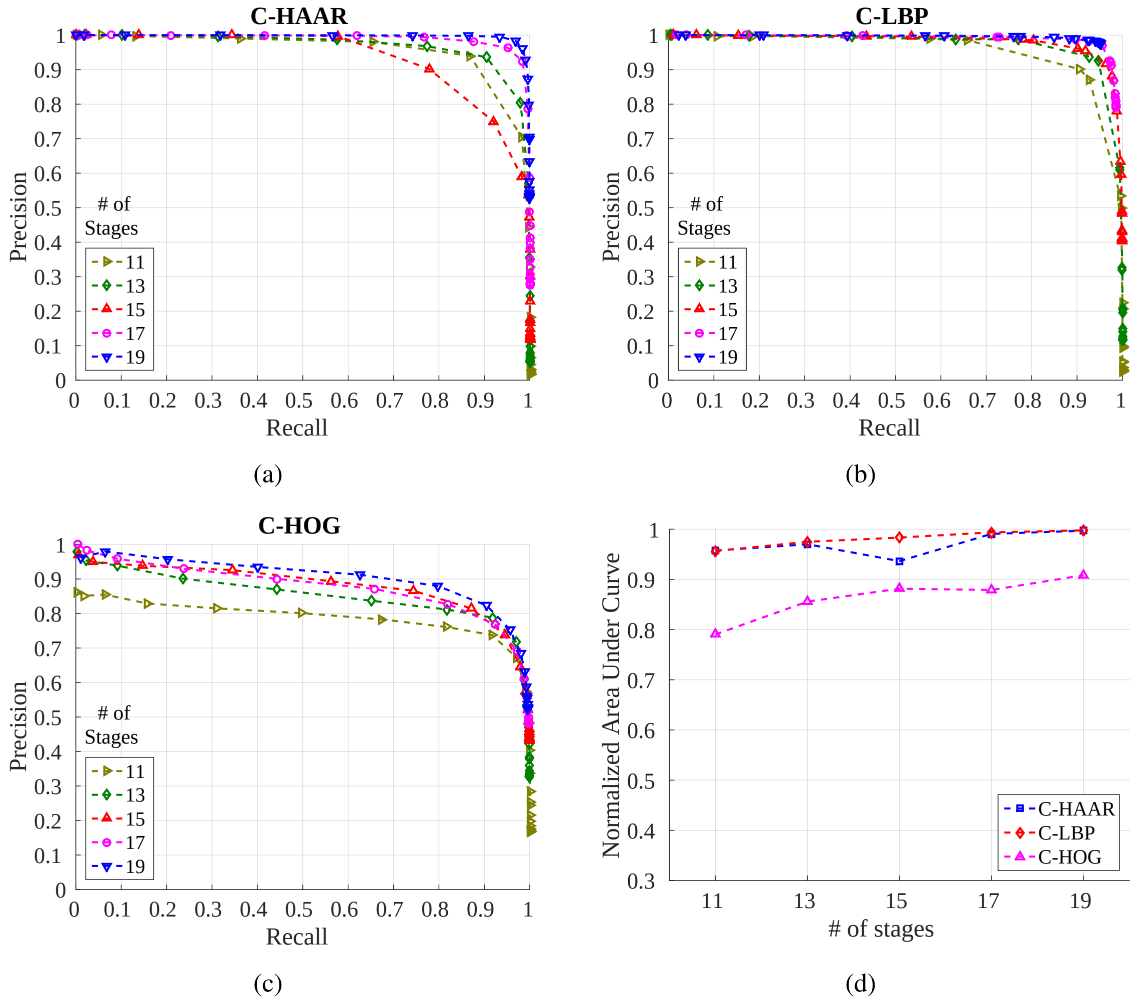

Figure 11. PR curves showing the performance of (a) C-HAAR, (b) C-LBP and (c) C-HOG for different number of stages on indoor test videos. (d) Normalized areas under the PR curves in (a), (b) and (c).

The performances of C-HAAR and C-LBP are close to each other in terms of maximum F-Scores (Table 3) and the normalized area under curve (Figure 11(d)), except for a decrease on stage 15 of C-HAAR, and they both perform better than C-HOG in all aspects. The lower performance of C-HOG is due to low number of features it extracts from a training window. Even with the extension of Zhu et al. [37], only 20 features are extracted from a 40×22-pixel^2 training image. For AdaBoost to estimate a better decision boundary, more features are required. The difference between the number of features used by C-HAAR and C-LBP, however, does not result in a considerable performance divergence.

We observe a slight difference between C-HAAR and C-LBP in terms of the lowest points that PR curves (Figure 11) reach. This is related with the performance differences between the methods at their

Table 3. Performance of the methods **indoors**, reported as F-Score values. Bold indicates best performances.

Feature Type	C-HAAR					C-LBP					C-HOG				
Number of Stages	11	13	15	17	19	11	13	15	17	19	11	13	15	17	19
Maximum F-Score	0.903	0.920	0.836	0.958	**0.976**	0.904	0.936	0.940	0.962	**0.964**	0.818	0.848	0.842	0.839	**0.862**
F-Score at Default Threshold	0.058	0.143	0.286	0.570	**0.822**	0.104	0.345	0.774	0.943	**0.954**	0.404	0.550	0.627	0.664	**0.716**

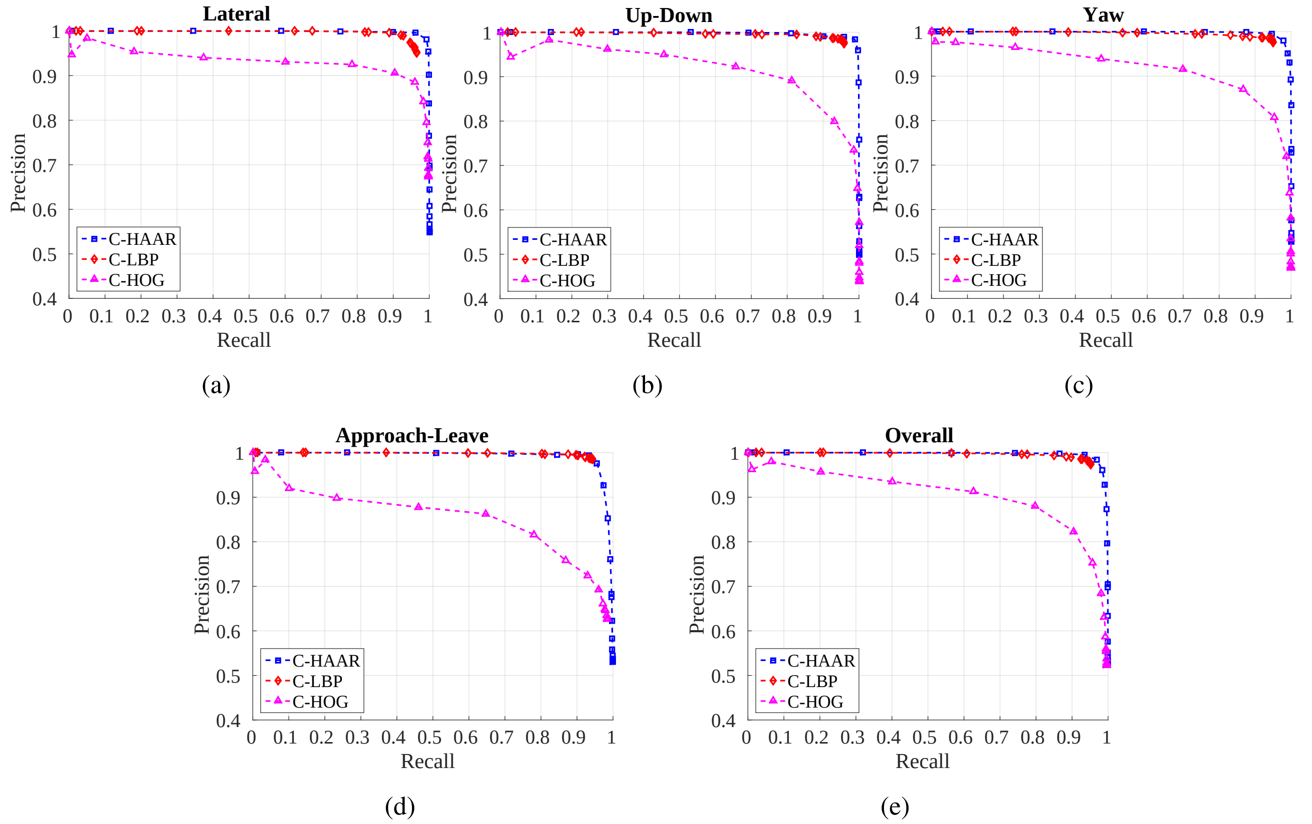

Figure 12. PR curves for (a) lateral left-to-right and right-to-left, (b) up and down, (c) yaw clockwise and counter-clockwise, (d) approach and leave, and (e) all motion types.

default threshold. As mentioned earlier, increasing the threshold of a classifier's latest stage, S to a very high value results in a classifier with a stage number of $S-1$. Therefore, since the performances of C-LBP classifiers at their default thresholds are greater than the default performances of C-HAAR classifiers, we observe PR curves ending at higher points in case of C-LBP.

For all the methods, training with 19 stages outperforms training with less stages. Therefore, taking 19 as the best stage number for all methods, we present their performances on different motion types in Figure 12 with their overall performances on all motion types. The performance of C-HAAR is slightly better than C-LBP on lateral, up-down and yaw motions since it has PR curves closer to the rightmost top corner of the figures. C-HOG gives the worst performance in all motion types.

When we look at the performances of each method individually for each motion type, C-HAAR performs similar on lateral, up-down and yaw motions, however its performance diminishes on approach-leave which is the most challenging motion in the indoor dataset. C-LBP has a performance degrade on lateral motion showing that it is slightly affected from the large background changes. Other than this, the performance of C-LBP is almost equal in other motion types. C-HOG performs better on lateral than other motions. A notable performance degrade is observed on approach-leave motion.

5.3. Outdoor Evaluation

We evaluated the classifiers trained with the outdoor training dataset using all outdoor motion types, namely, calm, agile and moving-background. We present the resulting PR curves and the normalized area under curves for each motion in Figure 13 and for overall performance in Figure 14. The F-Score performances are listed in Table 4.

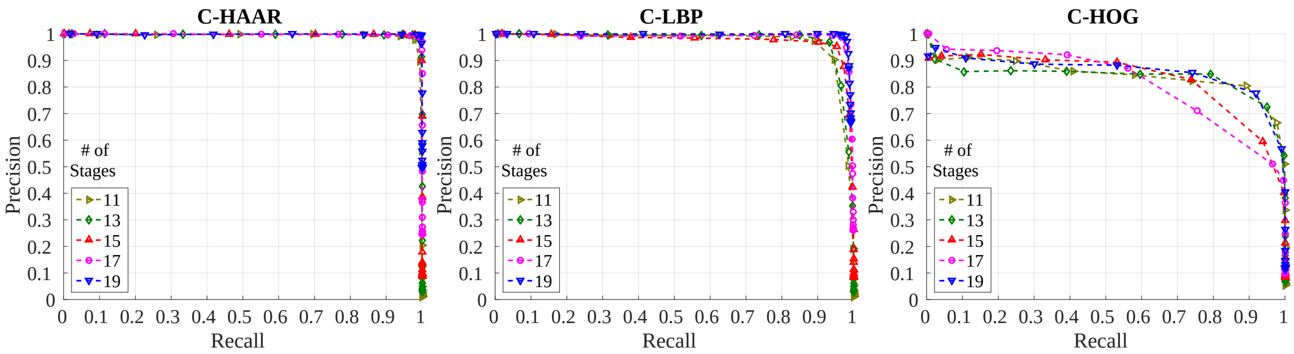

(a) Performances for calm test video.

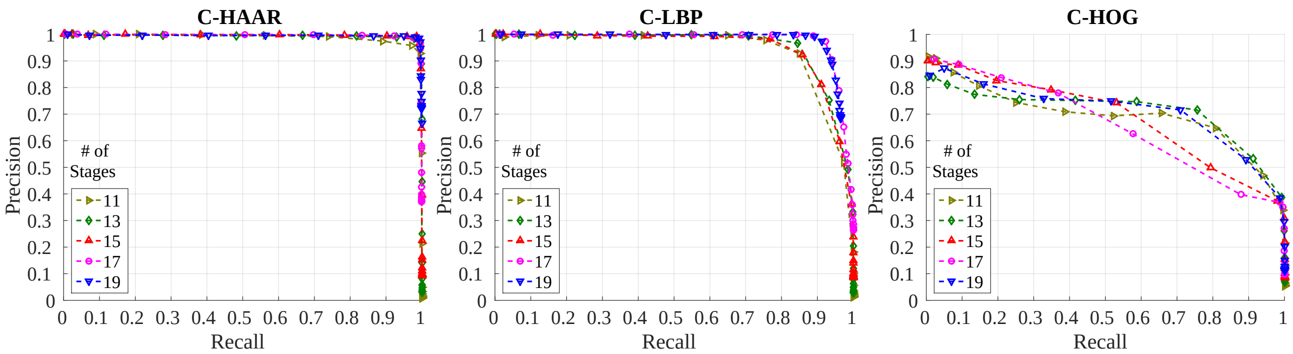

(b) Performances for agile test video.

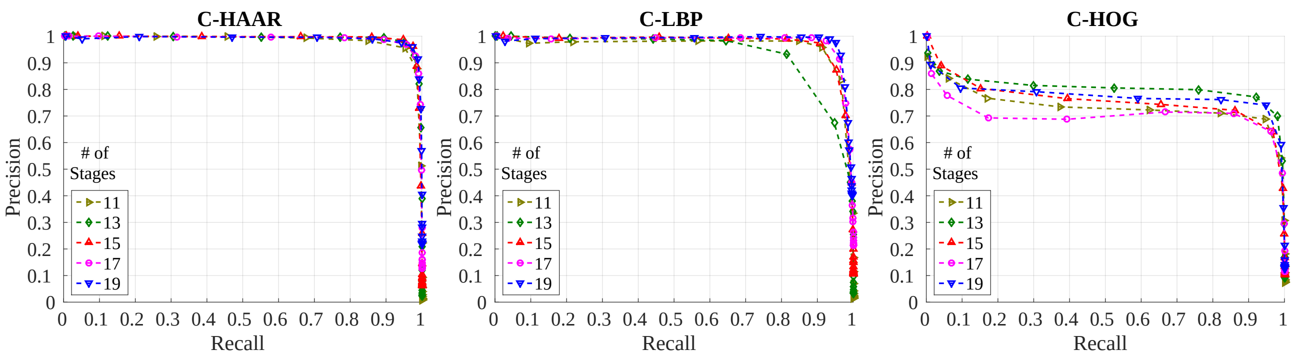

(c) Performances for moving background test video.

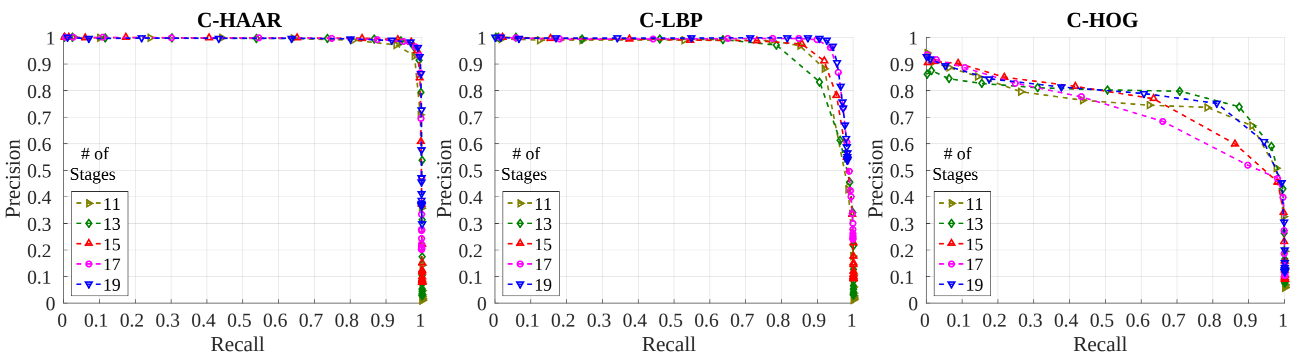

(d) Overall performances

Figure 13. PR curves for outdoor evaluation (Best viewed in color).

We notice that the performances of C-HAAR and C-LBP are remarkably better than C-HOG in all experiments. When comparing C-HAAR and C-LBP, C-HAAR is giving slightly better results in terms of all measures. Under agile maneuvers of the quadrotor, C-LBP and C-HOG display a performance degrade, while C-HAAR's performance is hardly affected. This suggests that C-HAAR is more robust against appearance changes due to rotation of the quadrotor. Slight performance decreases are observed in moving-background video for C-HAAR and C-LBP.

When compared to the indoor evaluation, C-HAAR classifiers with low stage numbers perform better outdoors. The performance of C-HOG decreases in outdoor tests. In terms of F-Score, best performing stage numbers differ for C-HAAR and C-HOG. Unlike indoors, the performances of C-LBP and C-HAAR classifiers at their default thresholds are close to each other, resulting in PR curves reaching to closer end points when compared to indoor results.

In order to determine the maximum distances at which the classifiers can detect the quadrotor successfully, an experiment is conducted with distance test video using best performing classifiers on the overall according to the F-Scores in Table 4. In this experiment, minimum detection window size is set to 20×11. The resulting maximum detection distances are 25.71 m, 15.73 m and 24.19 m, respectively for C-HAAR, C-LBP and C-HOG.

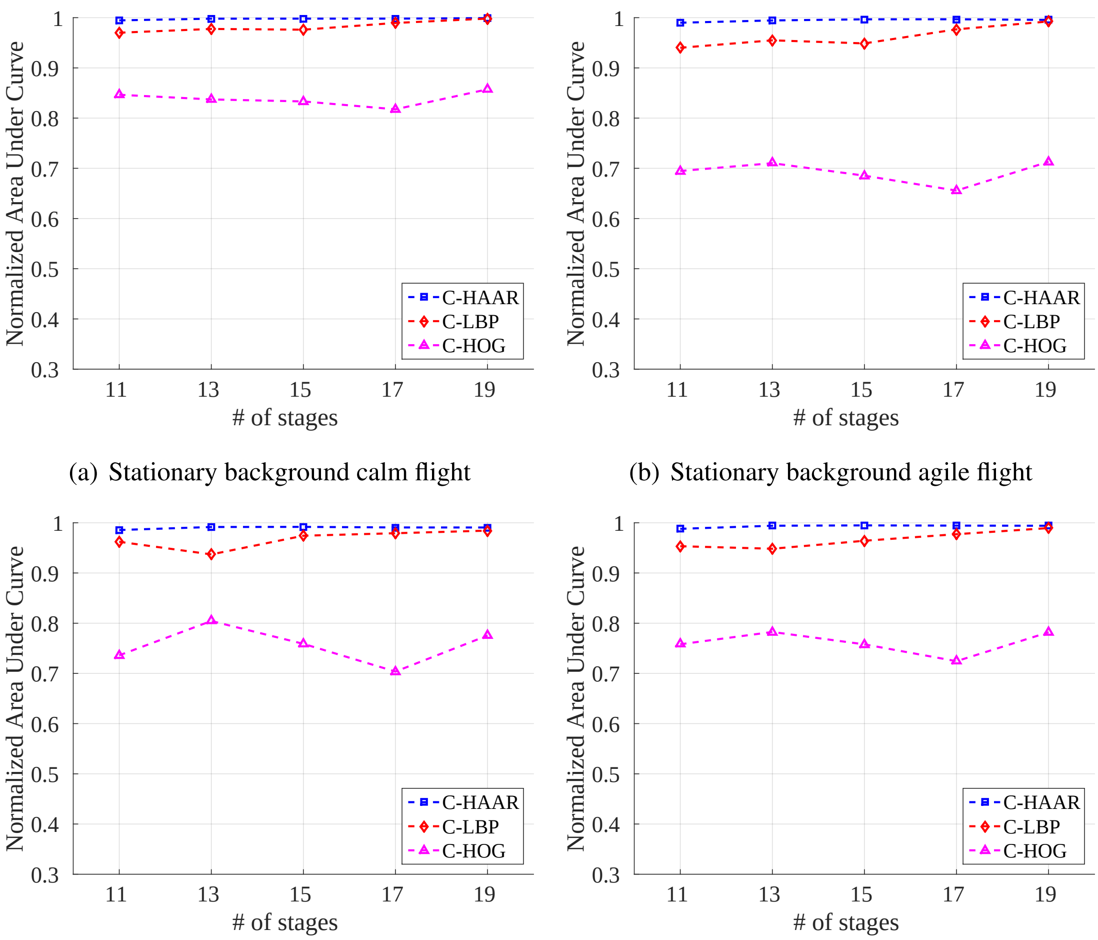

(a) Stationary background calm flight (b) Stationary background agile flight

(c) Moving background calm flight (d) All outdoor flights combined

Figure 14. Normalized area under curves for outdoor evaluation.

Table 4. Performance of the methods **outdoors**, reported as F-Score values. Bold indicates best performances.

	Feature Type	C-HAAR					C-LBP					C-HOG				
	Number of Stages	11	13	15	17	19	11	13	15	17	19	11	13	15	17	19
CALM	Maximum F-Score	0.979	0.987	0.991	0.991	**0.997**	0.930	0.951	0.953	0.977	**0.985**	**0.846**	0.822	0.781	0.732	0.842
	F-Score at Default Threshold	0.036	0.112	0.248	0.536	**0.734**	0.040	0.095	0.266	0.670	**0.930**	**0.118**	0.144	0.168	0.189	0.216
AGILE	Maximum F-Score	0.965	0.983	0.988	0.987	**0.989**	0.887	0.902	0.890	**0.947**	0.942	0.719	**0.735**	0.619	0.600	0.713
	F-Score at Default Threshold	0.034	0.108	0.282	0.727	**0.906**	0.041	0.094	0.260	**0.704**	0.920	0.121	**0.146**	0.168	0.188	0.211
MOVING BACKGROUND	Maximum F-Score	0.955	0.965	**0.969**	0.963	0.967	0.935	0.870	0.940	0.954	**0.964**	0.797	**0.840**	0.785	0.777	0.832
	F-Score at Default Threshold	0.030	0.084	**0.169**	0.274	0.441	0.043	0.111	0.269	0.480	**0.747**	0.158	**0.180**	0.199	0.216	0.234
OVERALL	Maximum F-Score	0.955	0.972	**0.977**	0.973	0.975	0.906	0.869	0.915	0.949	**0.957**	0.770	**0.801**	0.707	0.672	0.781
	F-Score at Default Threshold	0.033	0.099	**0.221**	0.429	0.627	0.042	0.100	0.265	0.594	**0.850**	0.132	**0.157**	0.178	0.198	0.221

5.4. Performance under Motion Blur

We have tested the performance of the methods against motion blur in the images. We utilized a linear motion blur similar to the one used in [85,86]. A motion-blurred version of an image I is generated by convolving it with a filter k (i.e., $\tilde{I} = I * k$) which is defined as:

$$k(x,y) = \begin{cases} 1 & \text{if } y = d/2, \\ 0 & \text{otherwise,} \end{cases} \tag{29}$$

where d is the dimension of the kernel (*blur length*), determining the amount of motion blur, sampled from a Gaussian distribution $N(\mu = 0, \sigma)$, with μ and σ being the mean and the standard deviation, respectively. We applied this kernel to the video images after a rotation of θ radian (*blur angle*) chosen from a uniform distribution $U(0, \pi)$. For each frame of a video, a new kernel is generated in this manner, and it is applied to all pixels in that frame. Using this motion blur model, we generated blurred versions of all indoor test videos for 5 different values of σ, namely, 5, 10, 15, 20 and 25.

We tested the best performing classifiers having 19 stages and giving the maximum F-Scores in Table 3 on the blurred and original videos. The tests are performed on the indoor dataset only, for the sake of simplicity, since we do not expect a difference between the effects of motion blur in indoor and outdoors. The results depicting the change in F-Score, PR against the amount of motion blur are given Figure 15. We see that C-HAAR and C-LBP display a more robust behavior compared to C-HOG since the decreasing trend in their F-Score and recall values are slower than C-HOG. C-LBP performs better than C-HAAR in terms of F-Score and recall. However, the precision of C-HAAR and C-HOG increases slightly with the increasing amount of motion blur. The reason for this increase is the decrease in the number of false positives since they start to be identified as background by C-HAAR and C-HOG when there is more noise. However, this trend has a limit since, at some point, the noise causes major decrease in the number of true positives. Here, $\sigma = 25$ is the point where the precision of C-HAAR and C-HOG starts to decrease.

In the case of C-LBP, precision values are continuously decreasing due to increasing number of false positives. However, this degradation in precision is not so rapid. Moreover, the decreasing trend in the recall of C-LBP is slower than other methods. This slow decline rate in the recall is resulting from a high number of correct detections and a low number of incorrect rejections.

5.5. Distance Estimation

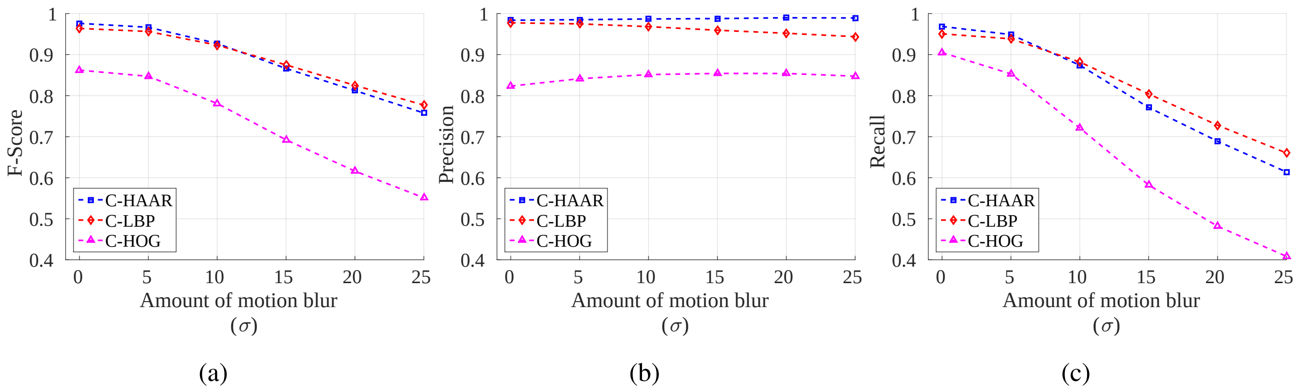

Figure 15. Performance of methods under motion blur. (a) F-Score, (b) Precision, and (c) Recall. To better illustrate the unexpected changes in precision and recall, they are plotted separately. $\sigma = 0$ corresponds to original videos without motion blur.

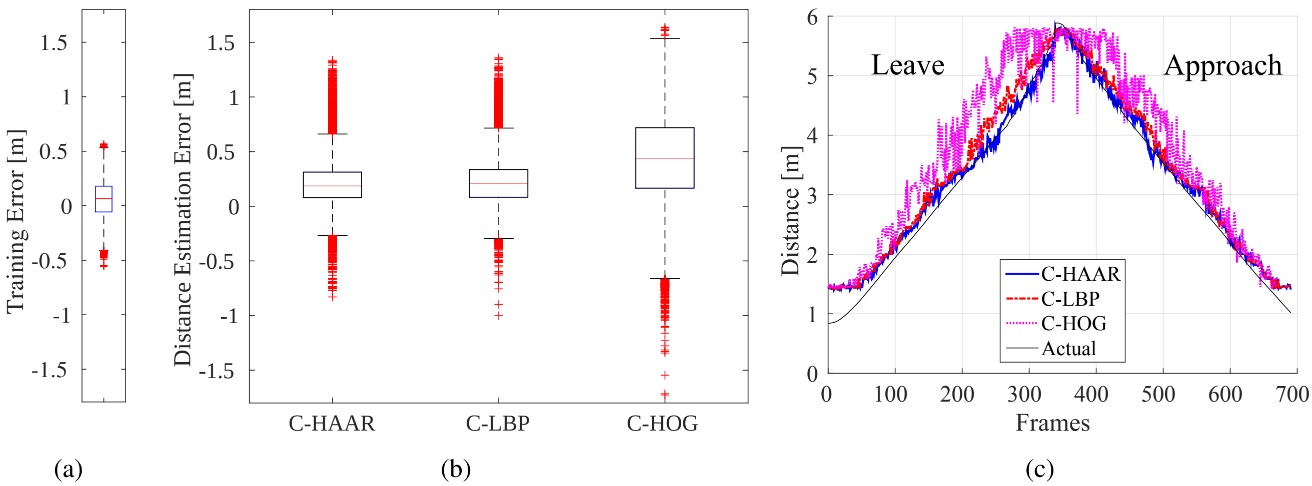

Figure 16. (a) Training error distribution for distance estimation. (b) Distribution of distance estimation error for each method. (c) Distance estimations during a leave motion followed by an approach.

To train the distance estimator (Section 3.5), we prepared a training set of 35570 pairs of $\{(w_i, h_i), d_i\}$, where w_i, h_i are the width and the height of the mUAV bounding box, respectively, and d_i is its known distance, acquired using the motion capture system (see Section 4 for the details).

A Support Vector Regressor (SVR) has been trained on this set with Radial Basis Functions kernel. The values of the parameters are optimized using a grid-search, yielding the following values: $\nu = 0.09, C = 0.1$, and $\gamma = 0.00225$. With these values and using 5-fold cross validation, a training error of 6.44 cm as median is obtained. The distribution of distance estimation errors over the training set is shown in Figure 16(a).

Since there is no ground truth distance information to hand for the outdoor dataset the distance estimation has been evaluated by means of indoor videos only.

As in motion-blur analysis, we tested the best performing classifiers having 19 stages resulting in maximum F-Scores tabulated in Table 3. The resulting distance estimation distributions are displayed in Figure 16(b).

We see that the performance of C-HAAR is slightly better than C-LBP. The medians of the error for C-HAAR and C-LBP are 18.6 cm and 20.83 cm, respectively. The performance of C-HOG is worse than the other two methods with a median error of 43.89 cm and with errors distributed over a larger span.

In Figure 16(c), we plot estimated and actual distances for a leave motion followed by an approach. These plots are consistent with the results provided with Figure 16(b) such that the performance C-HAAR and C-LBP are close to each other and better than C-HOG.

5.5.1. Time to Collision Estimation Analysis

We have analyzed the performance of the methods in the estimation of time to collision (TTC). In order to estimate TTC, the current speed (v_c) is estimated first:

$$v_c = \frac{d_c - d_p}{\Delta t}, \tag{30}$$

where d_c is current distance estimation, d_p is a previous distance estimation, and Δt is the time difference between two distance estimations. d_p is arbitrarily selected as the 90^{th} previous distance estimation to ensure a reliable speed estimation. Once v_c is calculated, TTC can be estimated as:

$$TTC = \frac{d_c}{v_c}. \tag{31}$$

Using this approach, we have evaluated the methods on indoor approach videos. Figure 17(a) shows the resulting box-plots for errors in estimating TTC. Figure 17(b) illustrates the estimated and actual TTC's for a single approach video. The performances of C-HAAR and C-LBP are close to each other with a smaller median error for C-LBP. C-HOG performs worse than C-HAAR and C-LBP as a result of its low performance in distance estimation.

5.6. Time Analysis

The training and testing time of the methods are analyzed in detail for the indoor and outdoor datasets on a computer with Intel® Core™ i7 860 @2.80 GHz processor. Currently, processors with similar computational power are available for mUAVs [87,88].

5.6.1. Training Time Analysis

Table 5. Time spent for training the cascaded classifiers having 19 stages in hours.

Feature Type	C-HAAR	C-LBP	C-HOG
Indoor	98.31	22.94	13.53
Outdoor	177.59	0.87	0.52

Figure 18 shows the amount of time required to train *each stage of the classifiers*, and Table 5 lists the total training times needed for the training of all 19 stages (the upper limit of 19 has been imposed due to the excessive time required for training C-HAAR). We observe that C-HAAR is the most time consuming method which is succeeded by C-LBP and C-HOG. It is observed that C-HAAR requires on the order of days for training, whereas C-LBP and C-HOG finish in even less than an hour.

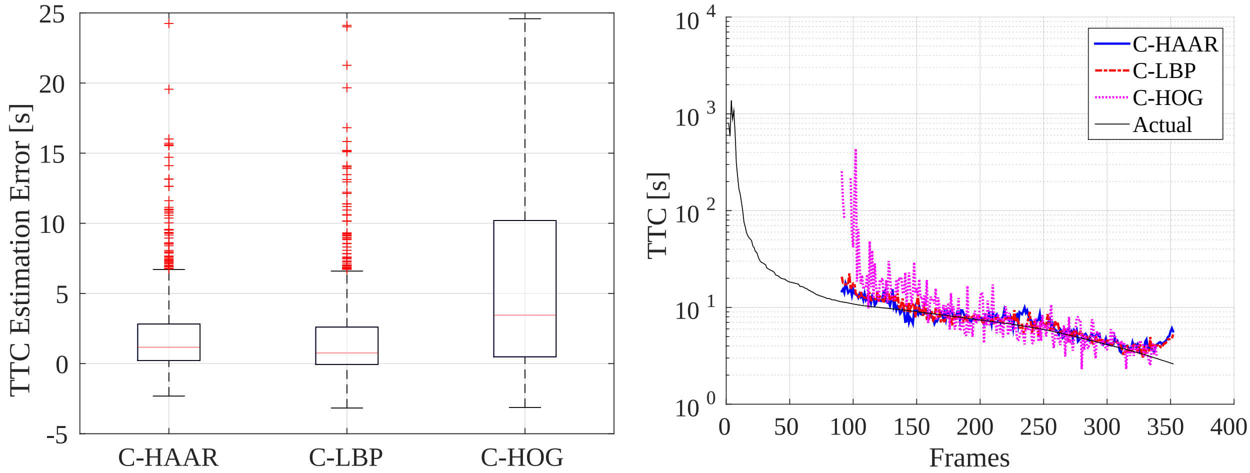

(a) (b)

Figure 17. Indoor time to collision estimation performances of the methods for (a) all approach motions, and (b) a single approach motion. In (a), there are outliers also outside the limits of the y-axis. However, in order to make differences between the methods observable, y-axis is limited between -5 and 25. In (b), the y-axis is in log-scale and no estimation is available until 90^{th} frame. The missing points after 90^{th} frame are due to negative or infinite time to collision estimations.

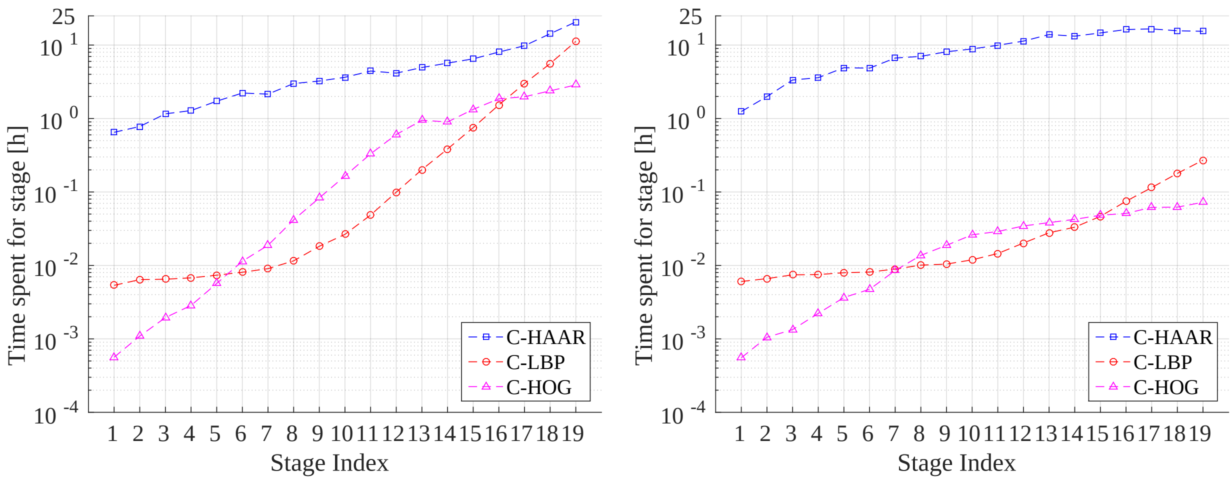

(a) (b)

Figure 18. (a) Indoor and (b) outdoor training times consumed for each stage in the cascaded classifier. The y-axes are in log-scale.

The main reason behind the differences in the training times of the methods is the number of features extracted by each method from an image window. As mentioned previously (Section 5.1), the ordering among the methods is C-HAAR, C-LBP and C-HOG with the decreasing number of associated features with an image window of 40×22 pixels. The increase in the number of features amounts to an increase in training the cascaded classifier to select the subset of good features via boosting.

We also observe significant difference between indoor and outdoor training times for each method. On the outdoor dataset, C-HAAR is twice slower than on the indoor dataset, where C-LBP and C-HOG are 26 times faster. The reason for this is the fact that the outdoor background images are more distinct, enabling C-LBP and C-HOG find the best classifier in each stage faster. However, this effect is not observed in C-HAAR since Haar-like features are adversely affected by the illumination changes which are observed substantially in our outdoor dataset.

5.6.2. Testing Time Analysis

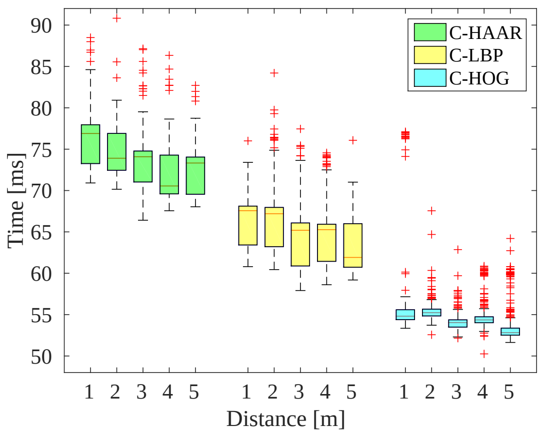

Figure 19. Change of computation time required to process one video frame with respect to distance of the quadrotor.

We have measured and analyzed the computation time of each method in two different aspects: i) on a subset of the indoor videos, we measured the computation time by changing the distance of the quadrotor to understand the effect of the distance. ii) we analyzed the average running times needed to process indoor and outdoor frames, with respect to the number of stages and the thresholds.

For the first experiment, we have selected 5 videos from yaw motion type for 1, 2, 3, 4 and 5 meter distances for middle-level height. In total, there were 1938 frames in these videos. We tested the performance of the classifiers having 19 stages at their default thresholds, as shown in Figure 19 with respect to the distance between the quadrotor and the camera. Although there are fluctuations, the time required to process a single frame shows an inverse correlation. This is so because as a quadrotor gets further away its footprint in the image will decrease and hence the bigger-scale detectors will reject the candidate windows faster which will yield a speed up in the overall detection.

In our second experiment, we tested the running time performance of the classifiers with respect to the number of stages. This has been performed both for the classifiers at their default threshold as well as with thresholds giving the maximum F-Score. Table 3 displays the results for indoor and Table 4 for outdoor.

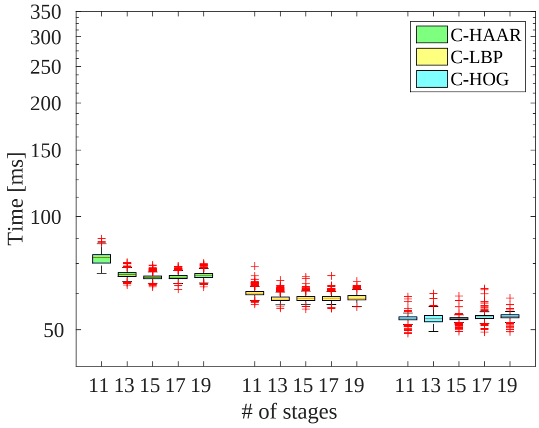

(a) Indoor tests with default thresholds

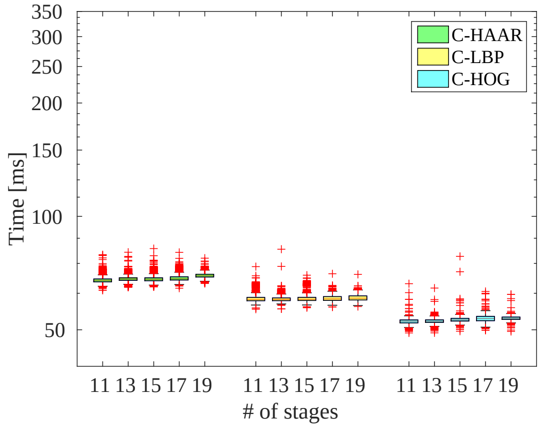

(b) Indoor tests with maximum F-score thresholds

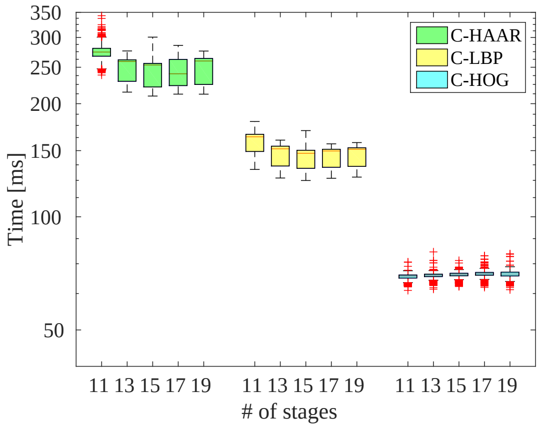

(c) Outdoor tests with default thresholds

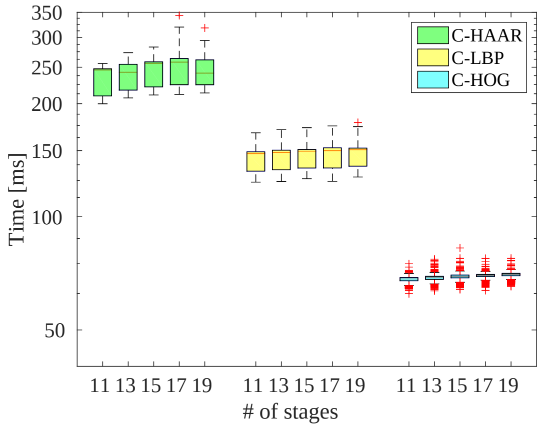

(d) Outdoor tests with maximum F-score thresholds

Figure 20. Analysis of time required to process one frame of (a-b) indoor and (c-d) outdoor videos. In (a) and (c), the classifiers are tested with their default thresholds, whereas in (b) and (d) the thresholds yielding maximum F-Score are used.

For indoor experiments, a subset of the indoor dataset consisting of videos from approach, down, lateral left-to-right and yaw-clockwise motion types containing 1366 frames in total was used. For the outdoor experiments, a total of 1500 frames from all motion types, namely calm, agile and moving-background, were used. Figure 20 displays the resulting time performance distributions.

When we compare indoor and outdoor results, we observe that all three methods require more time to process outdoor frames. This increase reaches up to three times for C-HAAR and C-LBP. Outdoor frames are bigger than indoor frames by a factor of 1.15. This accounts partially for the increase in the processing time. But the main reason is the higher complexity of outdoor background patterns, which manage to pass the early simple processing stages of the cascades more; thus consume more time before being identified as background.

When the results at the default thresholds and the maximum-F-score thresholds are compared, we observe an increase in the time spent on the lower stages of C-HAAR and C-LBP. This is due to the increasing number of candidate bounding boxes that are later merged into the resulting bounding boxes. Both detection and merging of these high number of candidate bounding boxes causes the processing time to increase.

For the maximum-F-score thresholds, processing time increases with the number of stages. This is an inherent result due to the increase in the number of stages.

The scatter plots in Figure 21 display the distribution of F-Scores with respect to the mean running times both for indoor and outdoor. The classifiers used in these plots are the ones giving maximum F-Scores. F-Score values for C-HAAR and C-LBP are close to each other and higher than C-HOG. For C-HAAR, F-Score values are spread over a larger range for indoors while the deviations in its mean time requirement increase for outdoor. Similar distributions are observed for C-LBP for both indoors and outdoors. F-Score values of C-HOG decrease and disperse over a wide range for outdoors, but the spread of its mean time requirements is very similar for indoors and outdoors.

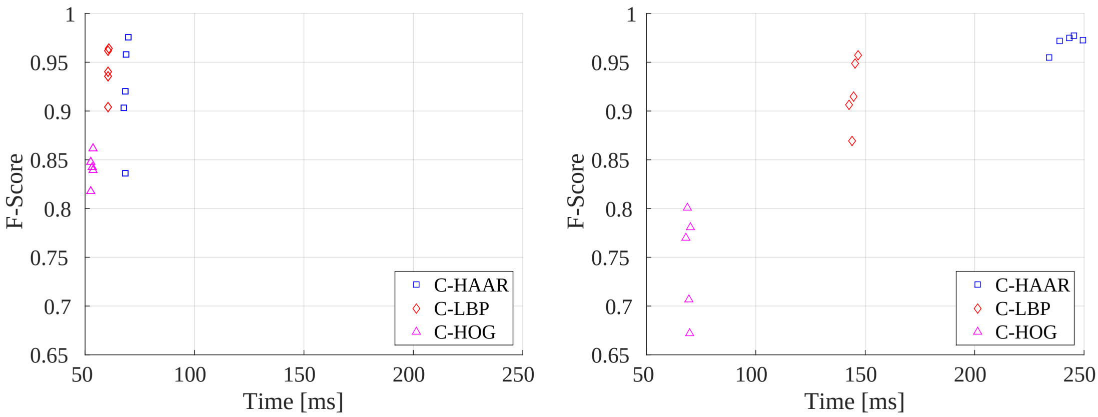

(a) (b)

Figure 21. (a) Indoor and (b) outdoor scatter plots for F-Score and mean running times. Each F-score value corresponds to a different classifier with different number of stages at the threshold resulting in maximum F-Score.

5.7. Sample Visual Results

In Figure 22, we present samples of successful detection and failure cases. These images are obtained using only the best performing C-LBP classifiers for the sake of space. C-LBP is remarkable among the three methods since its detection and distance estimation performance is very high and close to that of C-HAAR. Furthermore, it is computationally more efficient than C-HAAR both in training and testing. Three supplementary videos[5] are also available as addendum showing the detection performance of C-LBP on video sequences from the indoor and outdoor test datasets.

The images in Figure 22(a) display the performance of the detector in an indoor environment that has extensive T junctions and horizontal patterns. The performance of the detector under motion blur is also displayed. Outdoor images in Figure 22(b) exemplify outdoor performance of the detector where there are very complex textures including also moving-background patterns (pedestrians and various type of vehicles). When we look at the failures in Figure 22(c), we observe that the regions including T

[5] Available at: http://www.kovan.ceng.metu.edu.tr/∼fatih/sensors/

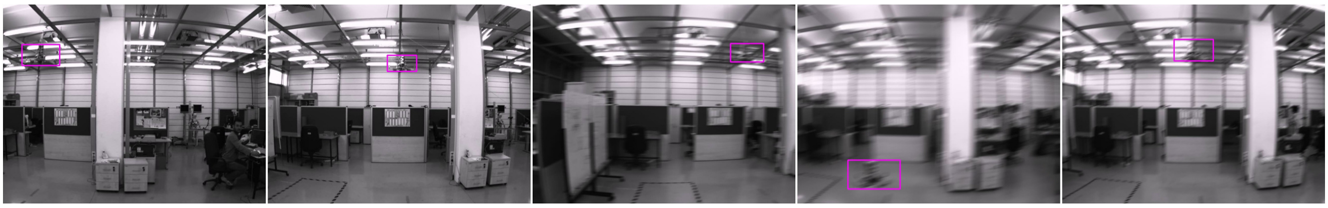

(a) Successful detections from indoor experiments.

(b) Successful detections from outdoor experiments.

(c) Failures from indoor and outdoor experiments.

Figure 22. Successful detection and failure examples from indoor and outdoor experiments obtained using best performing classifiers of C-LBP (only C-LBP results are provided for the sake of space).

junctions, horizontal patterns and silhouettes very similar to the quadrotor's are the confusing areas for the algorithms.

6. Conclusion

In this article, we have studied whether an mUAV can be detected and localized with a camera through cascaded classifiers using different feature types. To demonstrate this in a systematic manner, we performed several experiments indoors and outdoors. For indoor evaluations, a motion platform was built to analyze the performance of the methods in controlled motions, namely, in approach-leave, up-down, lateral and rotational motions. For outdoor evaluations, on the other hand, the methods were evaluated for cases where the mUAV was flown in a calm manner, agile manner or with other moving objects in the background. Maximum detection distance of the methods are also analyzed with an outdoor experiment.

We evaluated the performance of three methods, namely, C-HAAR, C-LBP and C-HOG where, in each method, a different feature extraction approach is combined with the boosted cascaded classifiers and with a distance estimator utilizing SVR. Our experiments showed that near real-time detection and accurate distance estimation of mUAVs are possible. C-LBP becomes prominent among the three methods due to its (1) high performance in detection, and distance and time to collusion estimation, (2) moderate computation time, (3) reasonable training time and (4) more robustness to the motion blur. When it comes to distance estimation, C-HAAR performs better since it positions the bounding boxes more accurately compared to the other methods. On the other hand, our time analysis reveals that C-HOG is the fastest both in training and testing.

We have demonstrated that an mUAV can be detected in about 60 ms indoors and 150 ms outdoors in images with 1032×778 and 1280×720 resolutions, respectively, with a detection rate of 0.96 F-Score both indoors and outdoors. Although this cannot be considered real-time, a real-time performance with cascaded classifiers is reachable, especially considering that the implementations are not optimized. We also showed that distance estimation of mUAVs is possible using simple geometric cues and the SVR even the change in the pose of the quadrotor or the camera results in different bounding boxes for the same distance between mUAV and the camera.

The performance of detection can be improved significantly when combined with tracking, e.g., by employing tracking-by-detection methods [89–91]. Such methods limit the search space of the detector in the next frame(s) by using the properties of the current and previous detections. This can improve both running time and the detection performance substantially.

Cascaded approaches are known to generalize rather well with the increase in the number of objects. By looking at simple, fast yet effective features at multiple stages to minimize false-positives and to maximize detection rates, successful applications on complex and challenging datasets with many many exemplars of the same class have been reported [36,37,92]. These indicate that, for mUAV detection, cascaded approaches are very suitable even if many mUAV variants with appearance characteristics are included.

Acknowledgments

Fatih Gökçe is currently enrolled in Faculty Development Program (ÖYP) on behalf of Süleyman Demirel University. For the experiments, we acknowledge the use of the facilities provided by the Modeling and Simulation Center of METU (MODSIMMER).

Author Contributions

Fatih Gökçe performed the experiments, Erol Şahin and Göktürk Üçoluk designed the experiments and provided the platforms, Fatih Gökçe and Sinan Kalkan wrote the paper.

Conflicts of Interest

The authors declare no conflict of interest.

References

1. Colomina, I.; Molina, P. Unmanned aerial systems for photogrammetry and remote sensing: A review. *{ISPRS} Journal of Photogrammetry and Remote Sensing* **2014**, *92*, 79 – 97.
2. Yuan, C.; Zhang, Y.; Liu, Z. A survey on technologies for automatic forest fire monitoring, detection, and fighting using unmanned aerial vehicles and remote sensing techniques. *Canadian Journal of Forest Research* **2015**, *45*, 783–792.
3. Ackerman, E. When Drone Delivery Makes Sense. *IEEE Spectrum*, 25 Sep 2014. Available: http://spectrum.ieee.org/automaton/robotics/aerial-robots/when-drone-delivery-makes-sense [Last accessed: 19 August 2015].

4. Holmes, K. Man detained outside White House for trying to fly drone. *CNN*, 15 May 2015. Available: http://edition.cnn.com/2015/05/14/politics/white-house-drone-arrest/ [Last accessed: 19 August 2015].
5. Martinez, M.; Vercammen, P.; Brumfield, B. Above spectacular wildfire on freeway rises new scourge: drones. *CNN*, 19 July 2015. Available: http://edition.cnn.com/2015/07/18/us/california-freeway-fire/ [Last accessed: 19 August 2015].
6. Andreopoulos, A.; Tsotsos, J.K. 50 Years of object recognition: Directions forward. *Computer Vision and Image Understanding* **2013**, *117*, 827–891.
7. Campbell, R.J.; Flynn, P.J. A survey of free-form object representation and recognition techniques. *Computer Vision and Image Understanding* **2001**, *81*, 166–210.
8. Lowe, D.G. Object recognition from local scale-invariant features. *International Conference on Computer Vision (ICCV)* **1999**, *2*, 1150–1157.
9. Belongie, S.; Malik, J.; Puzicha, J. Shape matching and object recognition using shape contexts. *IEEE Transactions on Pattern Analysis and Machine Intelligence* **2002**, *24*, 509–522.
10. Viola, P.; Jones, M. Rapid object detection using a boosted cascade of simple features. *IEEE Conference on Computer Vision and Pattern Recognition (CVPR)* **2001**, *1*, 511–518.
11. Dalal, N.; Triggs, B. Histograms of oriented gradients for human detection. *IEEE Conference on Computer Vision and Pattern Recognition (CVPR)* **2005**, *1*, 886–893.
12. Serre, T.; Wolf, L.; Bileschi, S.; Riesenhuber, M.; Poggio, T. Robust object recognition with cortex-like mechanisms. *IEEE Transactions on Pattern Analysis and Machine Intelligence* **2007**, *29*, 411–426.
13. Boutell, M.R.; Luo, J.; Shen, X.; Brown, C.M. Learning multi-label scene classification. *Pattern recognition* **2004**, *37*, 1757–1771.
14. Rosten, E.; Drummond, T. Machine Learning for High-Speed Corner Detection. *European Conference on Computer Vision (ECCV)* **2006**, *3951*, 430–443.
15. Trajkovic, M.; Hedley, M. Fast corner detection. *Image and Vision Computing* **1998**, *16*, 75–87.
16. Harris, C.; Stephens, M. A Combined Corner and Edge Detector. 4th Alvey Vision Conference, 1988, pp. 147–151.
17. Matas, J.; Chum, O.; Urban, M.; Pajdla, T. Robust Wide Baseline Stereo from Maximally Stable Extremal Regions. British Machine Vision Conference, 2002, pp. 36.1–36.10.
18. Shi, J.; Tomasi, C. Good features to track. IEEE Conference on Computer Vision and Pattern Recognition (CVPR), 1994, pp. 593–600.
19. Tuytelaars, T.; Mikolajczyk, K. Local invariant feature detectors: a survey. *Foundations and Trends® in Computer Graphics and Vision* **2008**, *3*, 177–280.
20. Bay, H.; Ess, A.; Tuytelaars, T.; Van Gool, L. Speeded-Up Robust Features (SURF). *Computer Vision and Image Understanding* **2008**, *110*, 346–359.
21. Lowe, D.G. Distinctive Image Features from Scale-Invariant Keypoints. *International Journal of Computer Vision* **2004**, *60*, 91–110.
22. Calonder, M.; Lepetit, V.; Strecha, C.; Fua, P. BRIEF: Binary Robust Independent Elementary Features. *European Conference on Computer Vision (ECCV)* **2010**, *6314*, 778–792.

23. Rublee, E.; Rabaud, V.; Konolige, K.; Bradski, G.R. ORB: An efficient alternative to SIFT or SURF. *International Conference on Computer Vision (ICCV)* **2011**, pp. 2564–2571.
24. Leutenegger, S.; Chli, M.; Siegwart, R.Y. BRISK: Binary Robust Invariant Scalable Keypoints. *International Conference on Computer Vision (ICCV)* **2011**, pp. 2548–2555.
25. Vandergheynst, P.; Ortiz, R.; Alahi, A. FREAK: Fast Retina Keypoint. *IEEE Conference on Computer Vision and Pattern Recognition (CVPR)* **2012**, *0*, 510–517.
26. Winn, J.; Criminisi, A.; Minka, T. Object categorization by learned universal visual dictionary. International Conference on Computer Vision (ICCV). IEEE, 2005, Vol. 2, pp. 1800–1807.
27. Murphy, K.; Torralba, A.; Eaton, D.; Freeman, W. Object detection and localization using local and global features. In *Toward Category-Level Object Recognition*; Springer, 2006; pp. 382–400.
28. Csurka, G.; Dance, C.R.; Fan, L.; Willamowski, J.; Bray, C. Visual categorization with bags of keypoints. Workshop on Statistical Learning in Computer Vision, ECCV, 2004, pp. 1–22.
29. Cortes, C.; Vapnik, V. Support-vector networks. *Machine learning* **1995**, *20*, 273–297.
30. Krizhevsky, A.; Sutskever, I.; Hinton, G.E. ImageNet Classification with Deep Convolutional Neural Networks. In *Advances in Neural Information Processing Systems (NIPS) 25*; Pereira, F.; Burges, C.; Bottou, L.; Weinberger, K., Eds.; Curran Associates, Inc., 2012; pp. 1097–1105.
31. LeCun, Y.; Bengio, Y.; Hinton, G. Deep learning. *Nature* **2015**, *521*, 436–444.
32. Dietterich, T.G. Ensemble methods in machine learning. In *Multiple classifier systems*; Springer, 2000; pp. 1–15.
33. Rowley, H.A.; Baluja, S.; Kanade, T. Neural network-based face detection. *IEEE Transactions on Pattern Analysis and Machine Intelligence* **1998**, *20*, 23–38.
34. Viola, P.; Jones, M.J. Robust real-time face detection. *International Journal of Computer Vision* **2004**, *57*, 137–154.
35. Freund, Y.; Schapire, R.E. A desicion-theoretic generalization of on-line learning and an application to boosting. Computational learning theory. Springer, 1995, pp. 23–37.
36. Liao, S.; Zhu, X.; Lei, Z.; Zhang, L.; Li, S.Z. Learning multi-scale block local binary patterns for face recognition. In *Advances in Biometrics*; Springer, 2007; pp. 828–837.
37. Zhu, Q.; Yeh, M.C.; Cheng, K.T.; Avidan, S. Fast human detection using a cascade of histograms of oriented gradients. *IEEE Conference on Computer Vision and Pattern Recognition (CVPR)* **2006**, *2*, 1491–1498.
38. Heredia, G.; Caballero, F.; Maza, I.; Merino, L.; Viguria, A.; Ollero, A. Multi-Unmanned Aerial Vehicle (UAV) Cooperative Fault Detection Employing Differential Global Positioning (DGPS), Inertial and Vision Sensors. *Sensors* **2009**, *9*, 7566–7579.
39. Hu, J.; Xie, L.; Xu, J.; Xu, Z. Multi-Agent Cooperative Target Search. *Sensors* **2014**, *14*, 9408–9428.
40. Rodriguez-Canosa, G.R.; Thomas, S.; del Cerro, J.; Barrientos, A.; MacDonald, B. A Real-Time Method to Detect and Track Moving Objects (DATMO) from Unmanned Aerial Vehicles (UAVs) Using a Single Camera. *Remote Sensing* **2012**, *4*, 1090–1111.
41. Doitsidis, L.; Weiss, S.; Renzaglia, A.; Achtelik, M.W.; Kosmatopoulos, E.; Siegwart, R.; Scaramuzza, D. Optimal Surveillance Coverage for Teams of Micro Aerial Vehicles in GPS-denied Environments Using Onboard Vision. *Auton. Robots* **2012**, *33*, 173–188.

42. Saska, M.; Chudoba, J.; Precil, L.; Thomas, J.; Loianno, G.; Tresnak, A.; Vonasek, V.; Kumar, V. Autonomous deployment of swarms of micro-aerial vehicles in cooperative surveillance. Unmanned Aircraft Systems (ICUAS), 2014 International Conference on, 2014, pp. 584–595.
43. Rosnell, T.; Honkavaara, E. Point Cloud Generation from Aerial Image Data Acquired by a Quadrocopter Type Micro Unmanned Aerial Vehicle and a Digital Still Camera. *Sensors* **2012**, *12*, 453–480.
44. Shen, S.; Mulgaonkar, Y.; Michael, N.; Kumar, V. Vision-based State Estimation for Autonomous Rotorcraft MAVs in Complex Environments. IEEE International Conference on Robotics and Automation (ICRA); , 2013.
45. Shen, S.; Mulgaonkar, Y.; Michael, N.; Kumar, V. Vision-Based State Estimation and Trajectory Control Towards Aggressive Flight with a Quadrotor. Robotics: Science and Systems (RSS); , 2013.
46. Shen, S.; Mulgaonkar, Y.; Michael, N.; Kumar, V. Initialization-Free Monocular Visual-Inertial Estimation with Application to Autonomous MAVs. International Symposium on Experimental Robotics, 2014.
47. Scaramuzza, D.; Achtelik, M.C.; Doitsidis, L.; Fraundorfer, F.; Kosmatopoulos, E.B.; Martinelli, A.; Achtelik, M.W.; Chli, M.; Chatzichristofis, S.A.; Kneip, L.; Gurdan, D.; Heng, L.; Lee, G.H.; Lynen, S.; Meier, L.; Pollefeys, M.; Renzaglia, A.; Siegwart, R.; Stumpf, J.C.; Tanskanen, P.; Troiani, C.; Weiss, S. Vision-Controlled Micro Flying Robots:from System Design to Autonomous Navigation and Mapping in GPS-denied Environments. *IEEE Robotics and Automation Magazine* **2014**. in press.
48. Achtelik, M.; Weiss, S.; Chli, M.; Dellaert, F.; Siegwart, R. Collaborative Stereo. Proceedings of the IEEE/RSJ Conference on Intelligent Robots and Systems (IROS), 2011, pp. 2242–2248.
49. Hesch, J.A.; Kottas, D.G.; Bowman, S.L.; Roumeliotis, S.I. Camera-IMU-based localization: Observability analysis and consistency improvement. *The International Journal of Robotics Research* **2013**.
50. Krajnik, T.; Nitsche, M.; Faigl, J.; Vanek, P.; Saska, M.; Preucil, L.; Duckett, T.; Mejail, M. A Practical Multirobot Localization System. *Journal of Intelligent & Robotic Systems* **2014**, *76*, 539–562.
51. Faigl, J.; Krajnik, T.; Chudoba, J.; Preucil, L.; Saska, M. Low-cost embedded system for relative localization in robotic swarms. IEEE International Conference on Robotics and Automation (ICRA), 2013, pp. 993–998.
52. Lin, F.; Peng, K.; Dong, X.; Zhao, S.; Chen, B. Vision-based formation for UAVs. IEEE International Conference on Control Automation (ICCA), 2014, pp. 1375–1380.
53. Zhang, M.; Lin, F.; Chen, B. Vision-based detection and pose estimation for formation of micro aerial vehicles. International Conference on Automation Robotics Vision (ICARCV), 2014, pp. 1473–1478.
54. Lai, J.; Mejias, L.; Ford, J.J. Airborne vision-based collision-detection system. *Journal of Field Robotics* **2011**, *28*, 137–157.

55. Petridis, S.; Geyer, C.; Singh, S. Learning to Detect Aircraft at Low Resolutions. In *Computer Vision Systems*; Gasteratos, A.; Vincze, M.; Tsotsos, J., Eds.; Springer Berlin Heidelberg, 2008; Vol. 5008, *Lecture Notes in Computer Science*, pp. 474–483.
56. Dey, D.; Geyer, C.; Singh, S.; Digioia, M. Passive, long-range detection of Aircraft: Towards a field deployable Sense and Avoid System. In Proceedings of Field and Service Robotics. Cambridge, MA, 2009.
57. Dey, D.; Geyer, C.; Singh, S.; Digioia, M. A cascaded method to detect aircraft in video imagery. *International Journal of Robotics Research* **2011**, *30*, 1527–1540.
58. Vásárhelyi, G.; Virágh, C.; Somorjai, G.; Tarcai, N.; Szorenyi, T.; Nepusz, T.; Vicsek, T. Outdoor flocking and formation flight with autonomous aerial robots. IEEE/RSJ International Conference on Intelligent Robots and Systems (IROS). IEEE, 2014, pp. 3866–3873.
59. Brewer, E.; Haentjens, G.; Gavrilets, V.; McGraw, G. A low SWaP implementation of high integrity relative navigation for small UAS. Position, Location and Navigation Symposium - PLANS 2014, 2014 IEEE/ION, 2014, pp. 1183–1187.
60. Roberts, J. Enabling Collective Operation of Indoor Flying Robots. PhD thesis, Ecole Polytechnique Federale de Lausanne (EPFL), 2011.
61. Roberts, J.; Stirling, T.; Zufferey, J.; Floreano, D. 3-D Relative Positioning Sensor for Indoor Flying Robots. *Autonomous Robots* **2012**, *33*, 5–20.
62. Stirling, T.; Roberts, J.; Zufferey, J.; Floreano, D. Indoor Navigation with a Swarm of Flying Robots. *IEEE International Conference on Robotics and Automation (ICRA)* **2012**.
63. Welsby, J.; Melhuish, C.; Lane, C.; Qy, B. Autonomous minimalist following in three dimensions: A study with small-scale dirigibles. In Proceedings of Towards Intelligent Mobile Robots, 2001.
64. Raharijaona, T.; Mignon, P.; Juston, R.; Kerhuel, L.; Viollet, S. HyperCube: A Small Lensless Position Sensing Device for the Tracking of Flickering Infrared LEDs. *Sensors* **2015**, *15*, 16484.
65. Etter, W.; Martin, P.; Mangharam, R. Cooperative Flight Guidance of Autonomous Unmanned Aerial Vehicles. *CPS Week Workshop on Networks of Cooperating Objects (CONET)* **2011**.
66. Basiri, M.; Schill, F.; Floreano, D.; Lima, P. Audio-based Relative Positioning System for Multiple Micro Air Vehicle Systems. Robotics: Science and Systems (RSS), 2013.
67. Tijs, E.; de Croon, G.; Wind, J.; Remes, B.; de Wagter, C.; de Bree, H.E.; Ruijsink, R. Hear-and-Avoid for Micro Air Vehicless. International Micro Air Vehicle Conference and Competitions (IMAV), 2010.
68. Nishitani, A.; Nishida, Y.; Mizoguch, H. Omnidirectional ultrasonic location sensor. IEEE Conference on Sensors, 2005.
69. Maxim, P.M.; Hettiarachchi, S.; Spears, W.M.; Spears, D.F.; Hamann, J.; Kunkel, T.; Speiser, C. Trilateration localization for multi-robot teams. Proceedings of the Sixth International Conference on Informatics in Control, Automation and Robotics, Special Session on MultiAgent Robotic Systems (ICINCO), 2008.
70. Rivard, F.; Bisson, J.; Michaud, F.; Letourneau, D. Ultrasonic relative positioning for multi-robot systems. IEEE International Conference on Robotics and Automation (ICRA), 2008, pp. 323 –328.

71. Moses, A.; Rutherford, M.; Valavanis, K. Radar-based detection and identification for miniature air vehicles. IEEE International Conference on Control Applications (CCA), 2011, pp. 933–940.
72. Moses, A.; Rutherford, M.J.; Kontitsis, M.; Valavanis, K.P. UAV-borne X-band radar for collision avoidance. *Robotica* **2014**, *32*, 97–114.
73. Lienhart, R.; Maydt, J. An extended set of Haar-like features for rapid object detection. International Conference on Image Processing, 2002, Vol. 1, pp. I–900–I–903 vol.1.
74. Papageorgiou, C.P.; Oren, M.; Poggio, T. A general framework for object detection. International Conference on Computer vision. IEEE, 1998, pp. 555–562.
75. Ojala, T.; Pietikainen, M.; Harwood, D. Performance evaluation of texture measures with classification based on Kullback discrimination of distributions. *12th IAPR Int. Conf. on Pattern Recognition* **1994**, *1*, 582–585.
76. Schölkopf, B.; Smola, A.J.; Williamson, R.C.; Bartlett, P.L. New support vector algorithms. *Neural computation* **2000**, *12*, 1207–1245.
77. 3DRobotics. Arducopter: Full-featured, open-source multicopter UAV controller. http://copter.ardupilot.com/ [Last accessed: 19 August 2015].
78. Gaschler, A. Real-Time Marker-Based Motion Tracking: Application to Kinematic Model Estimation of a Humanoid Robot. Master's thesis, Technische Universität München, Germany, 2011.
79. Gaschler, A.; Springer, M.; Rickert, M.; Knoll, A. Intuitive Robot Tasks with Augmented Reality and Virtual Obstacles. IEEE International Conference on Robotics and Automation (ICRA), 2014.
80. Horn, B.K.P.; Hilden, H.; Negahdaripour, S. Closed-Form Solution of Absolute Orientation using Orthonormal Matrices. *Journal of the Optical Society of America* **1988**, *5*, 1127–1135.
81. Umeyama, S. Least-squares estimation of transformation parameters between two point patterns. *IEEE Transactions on Pattern Analysis and Machine Intelligence* **1991**, *13*, 376–380.
82. Bradski, G. OpenCV. *Dr. Dobb's Journal of Software Tools* **2000**.
83. Kaewtrakulpong, P.; Bowden, R. An Improved Adaptive Background Mixture Model for Real-time Tracking with Shadow Detection. In *Video-Based Surveillance Systems*; Remagnino, P.; Jones, G.; Paragios, N.; Regazzoni, C., Eds.; Springer US, 2002; pp. 135–144.
84. Jaccard, P. The distribution of the flora in the Alpine zone. *New Phytologist* **1912**, *11*, 37–50.
85. Rekleitis, I.M. Visual Motion Estimation based on Motion Blur Interpretation. Master's thesis, School of Computer Science, McGill University, Montreal, Quebec, Canada, 1995.
86. Soe, A.K.; Zhang, X. A simple PSF parameters estimation method for the de-blurring of linear motion blurred images using wiener filter in OpenCV. International Conference on Systems and Informatics (ICSAI), 2012, pp. 1855–1860.
87. Hulens, D.; Verbeke, J.; Goedeme, T. How to Choose the Best Embedded Processing Platform for on-Board UAV Image Processing? Proceedings of the 10th International Conference on Computer Vision Theory and Applications, 2015, pp. 377–386.
88. AscendingTechnologies. AscTec Mastermind. http://www.asctec.de/en/asctec-mastermind/ [Last accessed: 19 August 2015].

89. Leibe, B.; Schindler, K.; Van Gool, L. Coupled detection and trajectory estimation for multi-object tracking. IEEE International Conference on Computer Vision (ICCV). IEEE, 2007, pp. 1–8.
90. Huang, C.; Wu, B.; Nevatia, R. Robust object tracking by hierarchical association of detection responses. In *European Conference on Computer Vision*; Springer, 2008; pp. 788–801.
91. Stalder, S.; Grabner, H.; Van Gool, L. Cascaded confidence filtering for improved tracking-by-detection. In *European Conference on Computer Vision*; Springer, 2010; pp. 369–382.
92. Dollar, P.; Wojek, C.; Schiele, B.; Perona, P. Pedestrian detection: An evaluation of the state of the art. *IEEE Transactions on Pattern Analysis and Machine Intelligence* **2012**, *34*, 743–761.